Ore Geology Reviews 81 (2017) 1287–1302

Contents lists available at ScienceDirect

Ore Geology Reviews

journal homepage: www.elsevier.com/locate/oregeorev

Metal source and tectonic setting of iron oxide-copper-gold (IOCG) deposits: Evidence from an in situ Nd isotope study of titanite from Norrbotten, Sweden

C.D. Storey [a,*], M.P. Smith [b]

[a] School of Earth and Environmental Science, University of Portsmouth, Portsmouth, UK
[b] School of Environment and Technology, University of Brighton, Brighton, UK

ARTICLE INFO

Article history:
Received 24 March 2016
Received in revised form 22 July 2016
Accepted 30 August 2016
Available online 1 September 2016

Keywords:
Titanite
Kiruna
Neodymium isotopes
IOCG deposits

ABSTRACT

Titanite occurs as a widespread accessory phase in mineralised zones and alteration associated with iron oxide-copper gold (IOCG) and iron oxide-apatite (IOA) deposits of Norrbotten County, Sweden, and is a major host of the REE in these deposits. In situ analyses of Sm—Nd isotope ratios in titanites previously analysed for U—Pb geochronology and trace element composition confirms previous interpretations of grain scale isotopic heterogeneity. Initial Nd-isotope ratios expressed relative to CHUR range from ~−3 to −8 in IOA deposits, from ~−1 to −9 in IOCG deposits, and from +2 to −4 in the most Cu-rich, deformed IOCG deposits of the Nautanen Deformation zone. Within individual IOA deposits ε_{Nd} varies relative to CHUR: from −3.1 to −4.0 at Valkommen (Malmberget), from −1.4 to −5.7 in grain cores, and −7.2 to −8.2 in grain rims rim at Gruvberget; and from −3.0 to −6.0 in grain cores and from −5.8 to −7.1 in grain rims at Luossavaara. In IOCG deposits at Rakkurijärvi ε_{Nd} varies from −6.1. to −7.1, and in deformed IOCG deposits at Nautanen from −1.3 to −2.3. These values are consistent with the derivation of the REE, and potentially economically enriched metals, from the local volcanic sequence, either via granitic melts, or directly by leaching by metasomatic fluids. The most Cu-rich deposits reflect the involvement of more basic protoliths. The age distribution of these deposits suggest IOA deposit formation during the collisional phase of the Svecofennian orogeny (~1.9–1.8 Ga), and IOCG mineralisation during this phase and during post-orogenic collapse (~1.8–1.7 Ga), whilst model ages indicate the ultimate enrichment of the continental crust in these metals during pre-collisional extensional and subduction-related basic magmatism. These processes underscore the importance of continental cycles both in producing the preserved geological record of orogenic ore deposition, and in the generation of fertile continental crust, from which metals can be mobilised by subsequent events.

1. Introduction

The iron oxide-copper-gold (IOCG) and related iron oxide-apatite (IOA; 'Kiruna type') class of mineral deposits (Hitzman et al., 1992; Hitzman, 2000; Williams et al., 2005) have been the subject of intense debate, in terms of both their classification and genetic mechanism. Whilst IOCG deposits are unequivocally hydrothermal in origin, models for the genesis of IOA deposits have ranged from magmatic crystallisation (e.g. Nyström, 1985; Nyström and Henríquez, 1994) to hydrothermal processes (e.g Parak, 1975) and metasomatic replacement (e.g. Bookstrom, 1995; Blake, 1990), although evidence is now mounting to support a hydrothermal origin (Barton, 2014). For both IOA and IOCG deposits the origin of mineralising fluids in hydrothermal models is problematic, with both magmatic-sourced brines (e.g. Pollard, 2006) and brines of surficial and possibly metaevaporitic origin (Barton and Johnson, 1996, 2000; Barton, 2014) both implicated. Again, evidence is now mounting to suggest mixing of a range of fluid sources (Kendrick et al., 2007; Kendrick et al., 2008; Gleeson and Smith, 2010). A critical part of these models must be to identify the source of metals, but studies in this area have been relatively limited. Gleason et al. (2000) showed that for IOCG/IOA systems ranging from Protoerozoic to Palaeogene in age the source of Nd determined from radioisotope systematics was in each case the pre-existing host igneous rocks rather than any specialised magmatic source. Mathur et al. (2002) used initial Os isotope ratios in magnetite to argue for contrasting metal sources in iron oxide-apatite (host sedimentary rocks) versus IOCG deposits (Cretaceous intrusive rocks) in the Chilean Iron Belt.

The IOA and IOCG deposits have also been highlighted in studies of the relationship of ore deposition to orogenic cycles, alongside 'orogenic' gold deposits (Goldfarb et al., 2010), because of an apparent

* Corresponding author.
E-mail addresses: Craig.Storey@portsmout.ac.uk (C.D. Storey), martin.smith@brighton.ac.uk (M.P. Smith).

http://dx.doi.org/10.1016/j.oregeorev.2016.08.035

correlation in the temporal distribution of deposits with the inferred record of supercontinent amalgamation (Groves et al., 2010). This is in contrast to deposits formed at ocean-continent subduction zones, notably porphyry copper and molybdenum systems, that show a temporal distribution strongly biased to the Cainozoic and Mesozoic (Groves et al., 2010). This has been attributed to the poor preservation potential for high crustal level metal deposits, such as porphyry coppers (Kesler and Wilkinson, 2008), whereas deposits in collision settings have a much higher preservation potential (Goldfarb et al., 2010). A similar argument has been developed in the investigation of the growth of the continental crust as recorded by peaks in the frequency of crystallisation ages of magmatic rocks (Condie, 1998), where an apparent correlation with inferred periods of supercontinent formation may reflect the increased preservation potential of rocks in collisional settings (Hawkesworth et al., 2009; Condie and Aster, 2010). In contrast, in arc settings facing an open ocean, tectonic erosion of the forearc and its accumulated sediments tends to proceed at rates approaching that of the magmatic flux forming new crust, resulting in no net growth of crust (Clift and Hartley, 2007). Groves et al. (2010) suggested that Precambrian examples of IOCG deposits formed 100–200 Ma after supercontinent assembly in extensional intra-cratonic environments related to anorogenic magmatism, whilst the IOA deposits formed in convergent margins prior to supercontinent assembly. Subcontinental lithospheric mantle (SCLM), fertilised during earlier subduction, was envisioned as a basic magma source, which drove crustal melting and was a potential source of metals for IOCG deposits. It also provided a bouyant medium, which resisted delamination and hence prevented uplift and erosion in districts where near-surface deposits are preserved. Richards and Mumin (2013) argued that the restriction of porphyry type systems to Phanerozoic rocks, and IOCG/IOA systems largely to the Precambrian reflected global changes in the ocean sulphate content and geothermal gradients at the end of the Precambrian. This led to a shift from S-poor arc magmas (and hence S-poor IOCG deposits) to S-rich arc magmas (and S-rich porphyry deposits) in the Phanerozoic. However, this hypothesis is critically dependent on a subdivision of the IOCG class into magmatic-hydrothermal systems, and systems with other fluid sources. If the class is viewed as a whole then the Precambrian/Phanerozoic time distinction is no longer apparent, although the apparent relationship to periods of collisional and accretionary tectonics is (Fig. 1). All these arguments critically depend on data on the temporal distribution of ore deposits and interpretations of metal and ligand source in the deposits themselves.

In this study we apply laser ablation multicollector ICP-MS (LA-MC-ICPMS) to the analysis of the Sm—Nd isotope systematics of titanite, previously analysed for U—Pb geochronology and trace element composition from hydrothermal alteration systems around IOCG and IOA deposits from Norrbotten County, Sweden (Fig. 2). Titanite is intimately associated with ore and alteration assemblages (Smith et al., 2007), and its REE patterns (Smith et al., 2009) are very similar to those of apatite from within the main magnetite ore body at Kirunavaara (Frietsch and Perdahl, 1995). Neodymium isotope ratios are used to investigate the potential REE sources in mineralisation, whilst model ages are used alongside a compilation of age-frequency relationships for magmatic rocks and mineral deposits from the region to examine the relationship of mineralisation to the tectonic evolution of the Svecokarelian orogeny.

2. Geological background

The IOCG and IOA deposits of Northern Sweden were formed in the period c.1.9 to 1.7 Ga (Romer et al., 1994, 1996; Wanhainen et al., 2005;

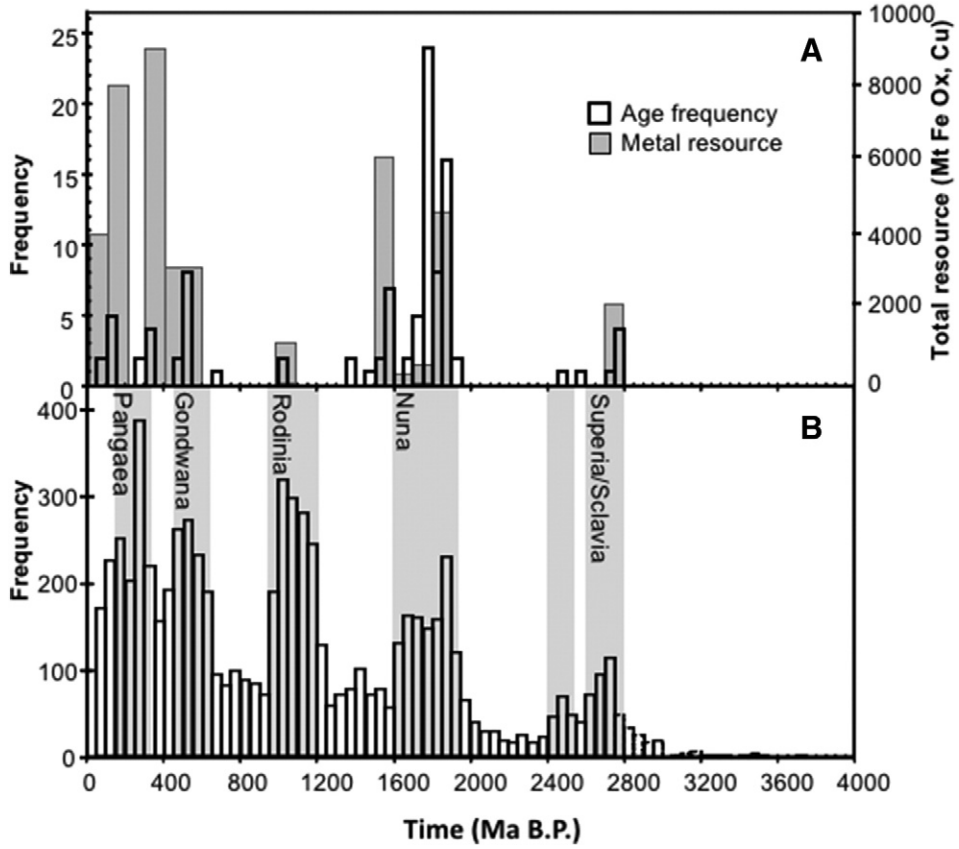

Fig. 1. (A) Compilation of IOCG deposits through time shown as histograms for frequency (open bars) and total metal resources (grey shaded bars). Modified from Williams et al. (2005) and Groves et al. (2010). (B) Compilation of detrital zircon ages from Australia from Campbell and Allen (2008). Also shown are inferred periods of supercontinental configuration.

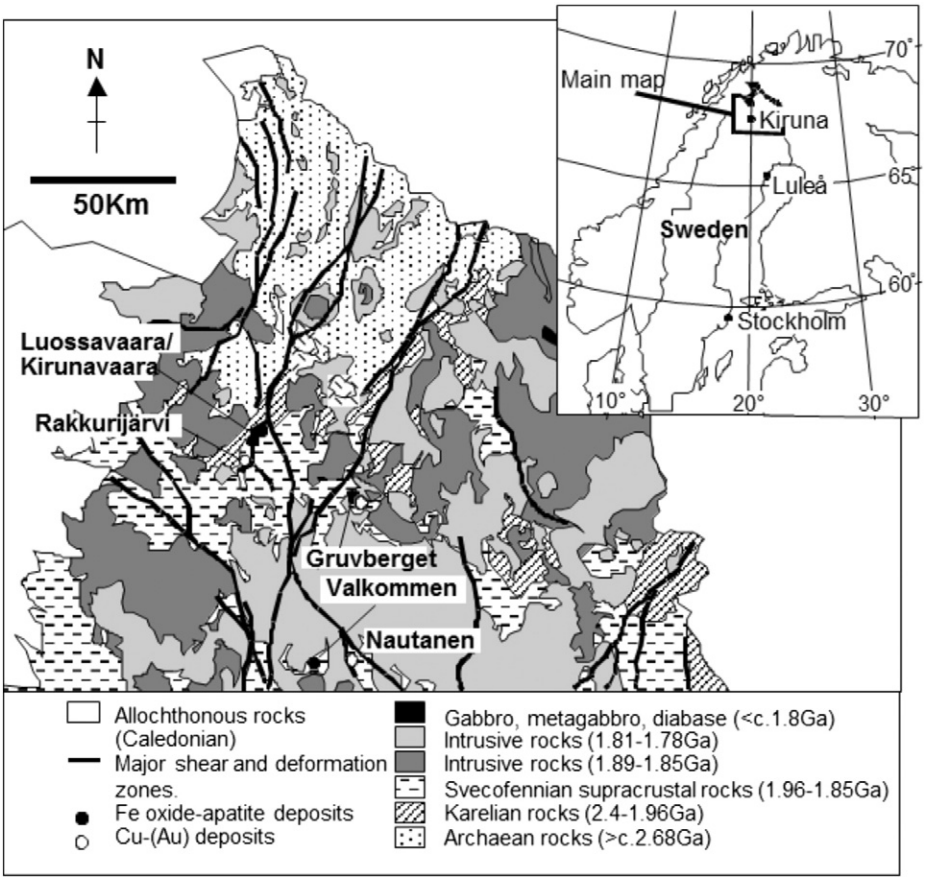

Fig. 2. Location map of Norrbotten county (inset), and simplified geological map of the study area based on Bergman et al. (2001) showing sample locations.

Smith et al., 2009). They are hosted within metavolcanic rocks of the Greenstone and Porphyry Groups, and temporally related to calc-alkaline (potentially subduction-related) granitoids (Haparanda and Perthite-Monzonite suites - 1.9–1.8 Ga; Skiöld, 1987), and two mica (linked to decompression melting during orogenic collapse) granites (Lina Suite – 1.79 Ga; Skiöld, 1988).

Rifting of the Archaean basement in the area and breakup of the preceding supercontinent began around 2.45 Ga, including the generation of large basic intrusions on the craton margins. The Greenstone Group was deposited in an extensional environment in the interval c.2.2–1.96 Ga (Bergman et al., 2001; Weihed et al., 2005). This period of magmatism was followed by the inception of an arc, and the eruption of associated volcanic rocks of potentially calc-alkaline character, with zircon U—Pb ages of ~1.8Ga, forming the porphyry group (Romer et al., 1994). The subsequent Svecokarelian orogeny resulted from accretion of this arc onto the Archaean craton in the period 1.9–1.8 Ga (Weihed et al., 2005). New geochronological work (Storey et al., 2007; Smith et al., 2009) within complex, zoned titanite crystals has suggested that the intermediate rocks of the Porphyry Group were contemporaneous with the latter stages of emplacement of the Greenstone Group, possibly via remelting of basic igneous crust as part of a bimodal volcanic sequence, from around 2.1 Ga, rather than generated during subsequent subduction, although this time period has not yet been confirmed by U—Pb analyses of zircon. The potential for resetting of zircon isotope systematics in the environs of the Kiruna deposit via dissolution-reprecipitation mechanisms (Putnis, 2002) is high, however, because of the extreme fluid conditions either during, or immediately after, ore formation (>400 °C, >2–3k bars, ~40 wt.% NaCl eq.; Broman and Martinsson, 2000; Smith et al., 2012). Evidence for evolved magmatic crust in the Svecofennian shield at around 2.0 Ga has been found in detrital zircon populations (Lahtinen et al., 2002). The preservation of older cores in titanite was possible because of the very large grain size (2–5 cm) compared to typical host rock zircon (200–300 μm). In the period 1.8–1.75 Ga post-orogenic granitoids of the Lina Suite were intruded and represent the final phase of continental amalgamation in this part of the world. Iron oxide-apatite (Kirunavaara, Malmberget) and IOCG mineralisation (Gruvberget, Rakkurijärvi) occurred during the Svecokarelian orogeny, and also during subsequent post-orogenic magmatism and deformation, which resulted in metamorphic and metasomatic overprints on earlier ores (Nautanen). The hydrothermal activity responsible for these mineralisation events manifested as new titanite and allanite growth, with clear distinctions in trace element chemistry (Smith et al., 2009). The samples used in this study are briefly described in Table 1.

3. Methods

Titanite and allanite unknowns were measured for Sm and Nd isotope ratios in-situ within polished sections 100 μm in thickness by laser ablation multi-collector ICPMS (LA-MC-ICPMS) at the University of Bristol. The thick sections were first imaged in a JEOL 5900LV scanning electron microscope using backscattered-electron (BSE) detection at the Natural History Museum, London. The BSE images were used to guide in-situ analysis within grains and all imaged grains and the analytical sites are shown in the Electronic Appendix. The laser used was a New-Wave UP193HE Excimer laser operating at 193 nm coupled to a Thermo Scientific Neptune MC-ICPMS. Operating conditions can be found in Table 2. Mass bias correction and isobaric interference of ^{144}Sm on ^{144}Nd were performed following the same methodology reported in Mcfarlane and McCulloch (2007). Two titanite standards

Table 1
Sample localities and descriptions.

Deposit	Sample number	Depth[a]	LA-ICPMS Reference[b]	Location Northing	Location Easting	Sample description	Titanite/allanite textural setting
IOA Deposits							
Luossavaara	03LUOSS01		LUOSS; L2	7538040	1685606	Magnetite-titanite veined and altered trachyandesite porphyry	0.5 cm titanite in amygdales with magnetite, actinolite, calcite and albite.
Gruvberget	03GRUV22		GRUV	7515145	1719960	Potassic (epidote-actinolite-K-feldspar) altered metavolcanic rock	1 cm titanite nucleated on rutile.
Malmberget (Valkommen)	03VALK01		VALK	7462074	1708551	Actinolite-feldspar-quartz-magnetite vein cutting potassic altered metavolcanic rock	1 cm titanite in vein with apatite, magnetite, minor hematite.
IOCG Deposits							
Rakkurijärvi	01RAK006	183.0 m	RAK	7526507	1682450	Potassic alteration overprinting scapolitisation in meta-trachyandesite	Titanite and allanite in amygdales associated with apatite and biotite.
Deformed IOCG deposits							
Nautanen	NAU84012	159.9 m	NAU	7463871	1719900	Well foliated epidote-actinolite-albite schist with coarse titanite	1–2 mm titanite aligned with schistosity, allanite as zones and cores in epidote.

[a] For drill core samples.
[b] Swedish national grid (RT90) reference.

(SP-REN and SP-HUL), one NIST glass (610) standard and one allanite standard (DAI) have been previously characterised for $^{143}Nd/^{144}Nd$ and $^{147}Sm/^{144}Nd$ isotope ratios (Foster and Vance, 2006; Mcfarlane and McCulloch, 2007). Chips of these were mounted within epoxy resin and polished. These were used to tune the instrument and to check that measured isotope ratios were within analytical uncertainty of those values reported. For $^{143}Nd/^{144}Nd$ the values obtained using this method for all standards are within measured uncertainty of the reported values (SP-REN – 0.512252; SP-HUL – 0.512337; 610–0.511908; DAI – 0.512560) within each session (Table 3). Furthermore, the $^{145}Nd/^{144}Nd$ are all within measured uncertainty of the canonical value of 0.348415 measured by TIMS (Wasserburg et al., 1981; Table 3). The more difficult measurement to assess is the $^{147}Sm/^{144}Nd$, which is dependent on homogeneity of the crystal and glass standards as well as laser induced elemental fractionation. In this study it was found that titanite standards were on average 3–4% higher and NIST glass 1% higher than reported solution values, although these were from relatively large crystal fragments. For allanite only LA-MC-ICPMS values are reported and our measurements are around 6% lower than those reported by Mcfarlane and McCulloch (2007). Another way to assess our Sm/Nd measurements is to take crystals of a known U—Pb age and plot them on a Sm/Nd isochron (Fig. 3). A sample from Nautanen, containing coexisting titanite and allanite in the same thick section previously measured by LA-ICPMS, gave a concordant U—Pb age of 1777 ± 20 Ma ($N = 12$, MSWD = 2.3; Smith et al., 2009). The same sample measured here for Sm—Nd gave a 15 point isochron age of 1777 ± 27 Ma ($n = 15$, MSWD = 0.91; Fig. 3). This gives us confidence in our measurement, verified against independent U—Pb geochronology. However, we do maintain caution with respect to our Sm/Nd isotope ratios and therefore we have reported our values as not corrected for Sm/Nd fractionation, but we note that for all titanite analyses the $^{147}Sm/^{144}Nd$ could be up to 4% higher. This would affect the calculated εNd(t) and the $T_{DM/CHUR}$, but all in the same direction. For these particular samples, the resultant magnitude of this affect would be a lowering of εNd(t) by 1 to 1.5 units and concomitant increase in T_{DM} by 75 to 100 Ma. For allanite the apparent Sm/Nd fractionation has an opposite effect. It is difficult to assess accuracy based on the limited data available for the standard. We note again that the co-existing allanite and titanite isochron age (Fig. 3) is in agreement with the concordant U—Pb age from these grains. In comparison, using fractionation-corrected $^{147}Sm/^{144}Nd$ values in the isochron yields an age of 1614 ± 25 Ma. Therefore, we report the data both corrected and uncorrected for Sm/Nd value in Table 4.

The internal precision of $^{143}Nd/^{144}Nd$ largely reflects the concentration of Nd in the sample as well as the fact that some samples were analysed with different spot sizes (Table 4). Variability of this ratio during ablation was negligible and each time resolved profile was assessed and, if it was clear that any secondary mineral or zone was intersected or if the laser penetrated through the crystal into underlying resin, then that part of the analysis was discarded from final calculation. In practice, only the first part of the signal (between 1 and 10s of signal) was sometimes removed due to the laser being started too late and the first part of the analysis representing ingrowth of the signal due to incomplete coupling of the laser with the analyte up until that point. Only 3 analyses required shortening at the ends of the analyses due to ablating into a secondary part of the crystal with a different Nd isotope ratio. The number of integrations per analysis are listed in Table 4. Comparing the number of integrations per analysis with the analytical uncertainty, there is no obvious relationship. Therefore, the uncertainty is considered to be related to Nd concentration and/or spot size or Nd isotope variation within each respective crystal/analysis. Within titanite standard SP-REN, for a typical analysis using a spot size of 65 μm, a current of around 1.9 V was achieved for the ^{144}Nd beam, resulting in an internal precision on the $^{143}Nd/^{144}Nd$ ratio of c.50 ppm (2SE). Titanite standard SP-HUL is slightly less concentrated in Nd, giving a current of around 1.5 V on ^{144}Nd using identical conditions, resulting in a slightly poorer precision of around 60 ppm (2SE) on the $^{143}Nd/^{144}Nd$ ratio. In terms of $^{147}Sm/^{144}Nd$, this ratio was variable in an unpredictable fashion in all analyses such that homogeneous parts of the crystal cannot easily

Table 2
Operating conditions for laser and MC-ICPMS used for Sm—Nd isotope ratio measurements.

Laser		MC-ICPMS	
Model	New-Wave UP193HE	Model	Thermo-Scientific Neptune
Pulse width	c.20 ns	Forward power	1200 W
Repetition rate	4 Hz	Cones	X-cones
Power	70%	Auxiliary gas	15 l·min^{-1}
Fluence	5 J·cm^{-2}	He carrier gas	c.1 l·min^{-1}
Energy	1.2 mJ	Ar mixer gas	c.1 l·min^{-1}
Spot size	Variable	N_2 mixer gas	c.0.03 l·min^{-1}

Table 3
Sm—Nd isotope ratio data for standard reference materials measured during the analytical sessions.

Analysis	$^{146}Nd/^{144}Nd$	2SE	$^{143}Nd/^{144}Nd$	2SE	$^{145}Nd/^{144}Nd$	2SE	ENd143	2SE	$^{147}Sm/^{144}Nd$	2SE
Daibosatsu Allanite										
DAI-1	0.735469	0.000060	0.512566	0.000014	0.348415	0.000009	0.077579	0.000124	0.178269	0.001423
DAI-2	0.735597	0.000075	0.512573	0.000024	0.348416	0.000013	0.076651	0.000272	0.171354	0.001208
DAI-3	0.735466	0.000052	0.512567	0.000019	0.348422	0.000011	0.075539	0.000079	0.176719	0.001206
DAI-4	0.734870	0.000056	0.512577	0.000017	0.348419	0.000011	0.079513	0.000115	0.163571	0.000753
DAI-5	0.734817	0.000048	0.512560	0.000016	0.348412	0.000011	0.079976	0.000101	0.167910	0.000695
DAI-6	0.734856	0.000060	0.512578	0.000017	0.348413	0.000009	0.079143	0.000055	0.175864	0.000707
DAI-7	0.735055	0.000055	0.512564	0.000016	0.348422	0.000011	0.079592	0.000048	0.187632	0.001929
DAI-8	0.735032	0.000044	0.512553	0.000014	0.348408	0.000009	0.079325	0.000080	0.182651	0.001526
DAI-9	0.735056	0.000045	0.512573	0.000016	0.348417	0.000008	0.078950	0.000091	0.180978	0.001409
	Average		0.512568		0.348416		0.078474		0.176105	
	2SD		0.000016		0.000009		0.003060		0.015023	
DAI-1	0.735487	0.000059	0.512549	0.000017	0.348415	0.000011	0.078413	0.000102	0.249757	0.001744
DAI-2	0.735529	0.000051	0.512551	0.000016	0.348415	0.000010	0.078705	0.000106	0.250700	0.001779
DAI-3	0.735600	0.000055	0.512574	0.000015	0.348411	0.000010	0.078688	0.000092	0.249429	0.001705
DAI-4	0.734075	0.000043	0.512581	0.000017	0.348405	0.000011	0.079817	0.000046	0.148611	0.000615
DAI-5	0.734086	0.000042	0.512583	0.000017	0.348411	0.000010	0.079448	0.000029	0.149199	0.000334
DAI-6	0.734017	0.000039	0.512560	0.000017	0.348408	0.000011	0.080383	0.000101	0.150635	0.000951
	Average		0.512567		0.348411		0.079242		0.199722	
	2SD		0.000030		0.000008		0.001539		0.110082	
SP-REN Titanite										
SP-REN-1	0.735330	0.000109	0.512236	0.000036	0.348411	0.000024	0.136054	0.000099	0.266011	0.000528
SP-REN-2	0.735360	0.000127	0.512250	0.000039	0.348398	0.000024	0.135994	0.000095	0.265568	0.000525
SP-REN-3	0.735385	0.000117	0.512252	0.000037	0.348398	0.000027	0.135788	0.000076	0.264774	0.000440
SP-REN-4	0.734671	0.000138	0.512223	0.000039	0.348411	0.000026	0.135239	0.000088	0.262389	0.000599
SP-REN-5	0.734701	0.000139	0.512248	0.000041	0.348416	0.000029	0.135124	0.000055	0.263374	0.000473
SP-REN-6	0.734703	0.000138	0.512250	0.000036	0.348398	0.000026	0.136805	0.000355	0.267183	0.001245
	Average		0.512243		0.348405		0.135834		0.264883	
	2SD		0.000023		0.000016		0.001226		0.003526	
SP-REN-1	0.735427	0.000144	0.512238	0.000043	0.348398	0.000027	0.135181	0.000072	0.260388	0.000544
SP-REN-2	0.735433	0.000143	0.512233	0.000041	0.348412	0.000028	0.135135	0.000091	0.259831	0.000584
SP-REN-3	0.735448	0.000143	0.512257	0.000045	0.348412	0.000029	0.135148	0.000086	0.259841	0.000604
SP-REN-4	0.734002	0.000146	0.512274	0.000047	0.348401	0.000028	0.136057	0.000070	0.267923	0.000490
SP-REN-5	0.734022	0.000147	0.512260	0.000046	0.348398	0.000028	0.136215	0.000050	0.269155	0.000431
SP-REN-6	0.733978	0.000148	0.512242	0.000047	0.348403	0.000030	0.136266	0.000051	0.269444	0.000461
	Average		0.512251		0.348404		0.135667		0.264431	
	2SD		0.000031		0.000013		0.001131		0.009725	
SP-HUL Titanite										
SP-HUL-1	0.735344	0.000050	0.512316	0.000024	0.348404	0.000014	0.138311	0.000091	0.284613	0.000736
SP-HUL-2	0.735326	0.000058	0.512352	0.000023	0.348430	0.000016	0.138347	0.000086	0.284554	0.000749
SP-HUL-3	0.735334	0.000060	0.512336	0.000023	0.348395	0.000017	0.138762	0.000072	0.287377	0.000558
SP-HUL-4	0.734890	0.000062	0.512353	0.000025	0.348421	0.000016	0.138785	0.000084	0.286669	0.000625
SP-HUL-5	0.734729	0.000037	0.512335	0.000022	0.348421	0.000015	0.138878	0.000101	0.287567	0.000644
SP-HUL-6	0.734758	0.000046	0.512346	0.000024	0.348403	0.000017	0.138944	0.000048	0.288413	0.000349
	Average		0.512340		0.348412		0.138671		0.286532	
	2SD		0.000028		0.000027		0.000546		0.003217	
SP-HUL-1	0.735615	0.000106	0.512335	0.000034	0.348415	0.000024	0.138864	0.000080	0.287194	0.000503
SP-HUL-2	0.735571	0.000087	0.512350	0.000027	0.348414	0.000021	0.139570	0.000055	0.290821	0.000355
SP-HUL-3	0.735486	0.000133	0.512333	0.000039	0.348399	0.000025	0.139041	0.000037	0.289063	0.000329
SP-HUL-4	0.734065	0.000043	0.512352	0.000028	0.348413	0.000016	0.139567	0.000045	0.293248	0.000333
SP-HUL-5	0.734045	0.000041	0.512341	0.000026	0.348390	0.000018	0.139505	0.000043	0.292428	0.000391
SP-HUL-6	0.734012	0.000038	0.512325	0.000026	0.348407	0.000018	0.139386	0.000050	0.291550	0.000445
	Average		0.512339		0.348406		0.139322		0.290717	
	2SD		0.000021		0.000020		0.000599		0.004488	
NIST 610										
610-1	0.735358	0.000056	0.511905	0.000023	0.348409	0.000014	0.632777	0.000468	1.594446	0.003005
610-2	0.735434	0.000044	0.511936	0.000023	0.348418	0.000013	0.635294	0.000333	1.605395	0.002778
610-3	0.735384	0.000039	0.511901	0.000025	0.348415	0.000013	0.634162	0.000303	1.603505	0.002676
610-4	0.734705	0.000056	0.511906	0.000028	0.348428	0.000016	0.633614	0.000686	1.601826	0.003082
610-5	0.734775	0.000051	0.511923	0.000022	0.348412	0.000014	0.637688	0.000532	1.620906	0.001595
610-6	0.734782	0.000047	0.511899	0.000024	0.348410	0.000015	0.638053	0.000962	1.624512	0.003264
	Average		0.511912		0.348415		0.635265		1.608432	
	2SD		0.000029		0.000014		0.004362		0.023442	
610-1	0.735427	0.000057	0.511904	0.000029	0.348414	0.000015	0.631543	0.000538	1.588923	0.001425
610-2	0.735478	0.000047	0.511934	0.000022	0.348425	0.000014	0.629670	0.000547	1.580349	0.002535
610-3	0.735410	0.000050	0.511897	0.000025	0.348398	0.000014	0.628999	0.000708	1.577071	0.002740
	Average		0.511912		0.348412		0.630071		1.582114	
	2SD		0.000039		0.000027		0.002637		0.012240	

be identified and meaning that any laser induced elemental fractionation between Sm and Nd during ablation cannot be recognised and corrected for. This results in a poorer internal precision than for $^{143}Nd/^{144}Nd$. SP-REN (same conditions as above) typically had internal precision of 0.1% (2SE), whereas SP-HUL has less variable Sm/Nd and had internal precision of around 3–400 ppm (2SE).

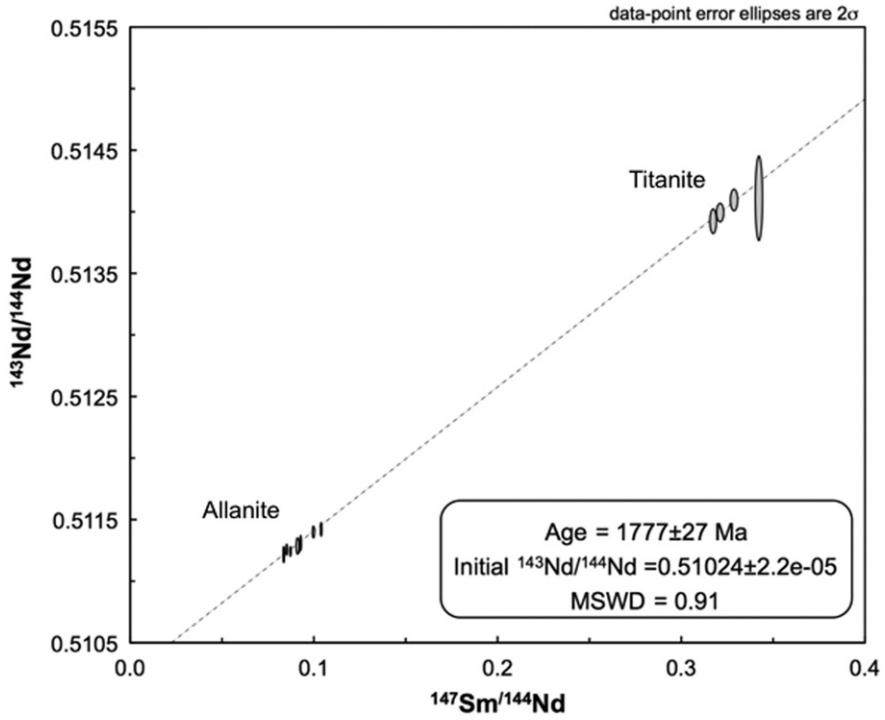

Fig. 3. Sm—Nd isochron of titanite and allanite from sample at Nautanen. The main cluster of analyses with $^{147}Sm/^{144}Nd$ around 0.1 are allanite and those with $^{147}Sm/^{144}Nd > 0.3$ are titanite.

4. Results

4.1. Petrography of titanite and allanite

The titanite and allanite used in this study come from the IOA deposits at Kirunavaara, Malmberget and Gruvberget, and the IOCG deposits at Rakkurijärvi (Table 1; Smith et al., 2009) and Nautanen (Martinsson, 2004). Kirunavaara consists of ~2 billion tonnes of magnetite-rich ore with subsidiary apatite, actinolite and hematite. The ore is generally massive with brecciated zones at the margins (Fig. 4A). The titanite sample comes from sodic and potassic altered intermediate lava immediately at the contact with the ore body at Luossavaara (Fig. 4B), where titanite is hosted in formerly amygdaloidal vug space, intergrown with magnetite and actinolite (Fig. 4C). Malmberget has mineralogical similarities to Kirunavaara, but has been subjected to higher grades of metamorphism, and is intensely deformed and segmented into multiple ore bodies (Martinsson, 2004). Titanite was sampled from the immediate hanging wall to the Valkommen ore body. Gruvberget is a deposit transitional between IOA and IOCG types, with Cu mineralisation overprinting a magnetite-hematite-apatite ore body. Titanite was sample from Na-altered metavolcanic rocks within 5 m of the main ore zone (Fig. 4D). In this case titanite occurs as BSE-dark cores overgrowing skeletal rutile, overgrown in turn by oscillatory zoned rims. At Rakkurijarvi chalcopyrite mineralisation occurs in the matrix to shear zone-hosted, magnetite and lithic breccias, associated with sodic and potassic altered trachyandesitic lavas (Fig. 4E). Allanite and titanite were sampled from amygdaloidal vug space within the altered lavas. At Nautanen allanite and titanite occur within strongly shear foliated metavolcanic rocks (Fig. 4F), showing a range of alteration types associated with vein-hosted chalcopyrite mineralisation (Martinsson, 2004). The details and previous U—Pb geochronology and trace element data for all samples are available in Smith et al. (2009).

Both titanite and allanite come from wall rock metasomatised settings that can be paragentically and geochemically linked to oxide or sulphide ore formation (Figs. 5, 6). At both Luossavaara and Rakkurijärvi the studied titanites and allanites occur within amygdales within altered lava, intergrown and apparently co-genetic with magnetite (Figs. 5A, 6A) and at Rakkurijärvi with later pyrite and chalcopyrite (Figs. 5B, 6C, D). Titanite at Valkommen overgrows apatite and is intergrown with magnetite (Fig. 6B). At Nautanen titanite occurs alongside pyrite and chalcopyrite, and overgrows pyrite in places (Fig. 6E). In general these textures indicate titanite formation was usually synchronous with magnetite deposition, and followed by sulphide mineralisation, whilst at Nautanen titanite growth was synchronous with sulphide mineralisation.

The trace element chemistry of titanite and allanite was discussed by Smith et al. (2009), and all data on the samples analysed here are available in that publication. The variation in trace element chemistry at Luossavaara and Gruvberget confirms the two stage growth history (Figs. 7, 8). The co-variation of the REE (represented by Nd) and selected transition metals is shown in Fig. 8. Copper contents are generally low (Fig. 8A), but both Ni and Mo (as sulphide associated metals) correlate with the Nd content (Fig. 8B, C). The highest values are reached at Valkommen for Ni and Gruvberget for Mo, suggesting distinctions in metal source that are supported by Nd isotope data. Vanadium tends to decrease with increasing REE content, except at Gruvberget again suggesting local variations in metal association and hence potential source.

4.2. Neodymium isotope systematics

The U—Pb systematics of titanite and allanite are summarised in Table 4, and full details are available in Storey et al. (2007) and Smith et al. (2009). We measured Sm—Nd isotopes within titanite and allanite formed within the ore deposits, in paragenetic settings described above. Examples of textural images and analytical locations are provide in Fig. 9, which also illustrates the complex internal zonation of titanite. Table 4 reports all Sm and Nd isotope ratios measured, and the locations of all analyses are shown in the Electronic Appendix.

In all cases, εNd(t, CHUR) in titanites and allanites from these deposits are slightly to highly negative (−1 to −8; Fig. 10A). Present

Table 4
Sm—Nd isotope data from titanite and allanite measured in-situ by laser ablation MC-ICPMS. Grain (c/r) - where applicable, c - core of grain, r - rim of grain; spot size - laser spot size used for analysis; age - age of crystallisation used for correction; N - number of integrated time slices within each run (maximum = 100) meas - measured isotope ratio uncorrected for fractionation; err 2se - measured uncertainty at 2 standard errors; (i) - isotope ratio corrected for age to initial composition at the time of crystallisation; (T0) - corrected to initial age of crystallisation; - CHUR - Chondritic Uniform Reservoir; (DM) - Depleted Mantle; 2 stage - 2 stage model age based on Sm/Nd ratio of 0.12; corr - isotope ratio corrected for fractionation (4% Sm/Nd fractionation).

Mineral	Grain (c/r)	Spot size (μm)	Age (Ma)	N	$^{147}Sm/^{144}Nd$ meas	$^{143}Nd/^{144}Nd$ meas	err 2se	$^{143}Nd/^{144}Nd$(i)	εNd(T0)	err 2se	Uncorrected Sm/Nd / εNd(T CHUR)	εNd(TDM)	T(DM) 2 stage	Corrected Sm/Nd / $^{147}Sm/^{144}Nd$ corr	$^{143}Nd/^{144}Nd$(i)	εNd (T CHUR)	εNd(TDM)	T(DM) 2 stage
Titanite	VALK A	65	1900	94	0.166794	0.511884	0.000042	0.509851	−11.1	0.4	−4.0	−7.9	2515	0.160379	0.510057	−2.4	−6.3	2392
Titanite	VALK B	65	1900	93	0.156337	0.511075	0.000130	0.509897	−13.4	0.5	−3.7	−7.7	2496	0.150324	0.510064	−2.3	−6.2	2382
Titanite	VALK C	50	1900	93	0.168218	0.511642	0.000027	0.509875	−10.8	0.4	−4.0	−7.9	2518	0.161748	0.510055	−2.4	−6.4	2395
Titanite	VALK D	50	1900	99	0.148022	0.512288	0.000029	0.509829	−15.0	0.4	−3.3	−7.2	2461	0.142329	0.510083	−1.9	−5.8	2352
Titanite	VALK E	30	1900	100	0.149298	0.512233	0.000023	0.509827	−14.9	0.4	−3.5	−7.5	2481	0.143556	0.510070	−2.1	−6.1	2372
Titanite	VALK F	50	1900	100	0.144018	0.511491	0.000046	0.509915	−15.8	0.4	−3.2	−7.1	2452	0.138479	0.510087	−1.8	−5.7	2347
Titanite	VALK G	50	1900	100	0.167924	0.511201	0.000040	0.509923	−10.6	0.6	−3.7	−7.7	2497	0.161465	0.510069	−2.2	−6.1	2374
Titanite	VALK H	50	1900	100	0.145488	0.511156	0.000033	0.509903	−15.4	0.4	−3.1	−7.0	2449	0.139892	0.510090	−1.8	−5.7	2342
Titanite	VALK I	50	1900	100	0.164751	0.511071	0.000027	0.509861	−11.5	0.5	−3.9	−7.8	2508	0.158414	0.510060	−2.3	−6.3	2388
Titanite	VALK J	50	1900	100	0.140237	0.511137	0.000026	0.509877	−16.7	0.4	−3.1	−7.0	2444	0.134843	0.510090	−1.7	−5.7	2341
Titanite	VALK K	50	1900	100	0.159309	0.511132	0.000026	0.509864	−12.8	0.4	−3.9	−7.8	2507	0.153182	0.510058	−2.4	−6.3	2391
Titanite	VALK L	50	1900	100	0.151017	0.511071	0.000020	0.509858	−14.5	0.4	−3.6	−7.5	2482	0.145209	0.510071	−2.1	−6.0	2371
Titanite	GRUV A - c	90	2050	87	0.051296	0.511113	0.000040	0.509903	−39.5	1.2	−1.4	−4.9	2430	0.049323	0.509938	−0.9	−4.4	2390
Titanite	GRUV B - r	65	1850	95	0.140074	0.510980	0.000022	0.509856	−20.7	0.7	−7.4	−11.5	2745	0.134687	0.509931	−6.1	−10.2	2645
Titanite	GRUV C - c	90	2050	96	0.099973	0.511205	0.000018	0.509895	−29.8	0.8	−4.6	−8.0	2673	0.096128	0.509804	−3.5	−7.0	2594
Titanite	GRUV D - r	65	1850	95	0.154357	0.511615	0.000063	0.509704	−17.5	0.5	−7.7	−11.8	2765	0.148420	0.509924	−6.3	−10.3	2655
Titanite	GRUV E - c	65	2050	98	0.117056	0.511645	0.000059	0.509728	−26.5	1.0	−5.7	−9.2	2764	0.112554	0.509753	−4.5	−8.0	2672
Titanite	GRUV F - c	90	2050	100	0.089122	0.511153	0.000019	0.509898	−32.8	1.9	−4.7	−8.1	2681	0.085694	0.509794	−3.7	−7.2	2610
Titanite	GRUV G - c	90	2050	100	0.105601	0.511451	0.000092	0.509823	−28.2	1.6	−4.4	−7.8	2660	0.101539	0.509816	−3.3	−6.8	2576
Titanite	GRUV H - r	65	1850	100	0.167020	0.511367	0.000030	0.509766	−14.6	0.8	−7.7	−11.8	2767	0.160597	0.509929	−6.2	−10.3	2648
Titanite	GRUV I - c	90	2050	100	0.087255	0.511122	0.000018	0.509894	−30.3	2.5	−1.7	−5.2	2452	0.083899	0.509943	−0.8	−4.3	2383
Titanite	GRUV J - r	65	1850	100	0.145160	0.511311	0.000036	0.509783	−19.3	0.5	−7.2	−11.3	2730	0.139577	0.509943	−5.9	−10.0	2627
Titanite	GRUV K - r	65	1850	100	0.201937	0.511368	0.000048	0.509830	−6.7	0.6	−8.1	−12.2	2799	0.194170	0.509924	−6.3	−10.3	2655
Titanite	GRUV L - r	65	1850	100	0.197579	0.511096	0.000017	0.509887	−7.8	0.5	−8.2	−12.2	2802	0.189980	0.509920	−6.4	−10.4	2661
Titanite	LUOSS A - r	90	1870	93	0.128077	0.511171	0.000017	0.509902	−22.2	0.9	−5.9	−10.0	2645	0.123151	0.509975	−4.8	−8.8	2553
Titanite	LUOSS B - r	90	1870	100	0.103871	0.511479	0.000028	0.509756	−27.9	0.8	−5.8	−9.8	2633	0.099876	0.509972	−4.8	−8.8	2558
Titanite	LUOSS C - r	65	1870	100	0.101853	0.511316	0.000084	0.509788	−28.7	0.6	−6.2	−10.2	2663	0.097935	0.509951	−5.2	−9.2	2589
Titanite	LUOSS D - r	65	1870	100	0.098323	0.511787	0.000044	0.509712	−30.4	0.5	−7.0	−11.0	2726	0.094541	0.509908	−6.1	−10.1	2655
Titanite	LUOSS E - r	65	1870	100	0.102332	0.511425	0.000049	0.509738	−29.1	0.5	−6.7	−10.7	2702	0.098396	0.509926	−5.7	−9.7	2628
Titanite	LUOSS F - r	65	1870	96	0.103044	0.512420	0.000057	0.509678	−29.2	0.5	−6.9	−10.9	2722	0.099081	0.509913	−6.0	−10.0	2647
Titanite	LUOSS G - r	65	1870	100	0.098557	0.511401	0.000024	0.509737	−30.4	0.4	−7.1	−11.1	2731	0.094766	0.509905	−6.1	−10.1	2660
Titanite	LUOSS H - r	65	1870	100	0.098344	0.511089	0.000022	0.509884	−29.6	0.8	−6.2	−10.2	2663	0.094561	0.509950	−5.3	−9.3	2592
Titanite	LUOSS I - r	65	1870	98	0.091320	0.510466	0.000032	0.509928	−32.2	0.4	−7.1	−11.1	2734	0.087808	0.509899	−6.3	−10.3	2669
Titanite	L2 A - r	90	1870	90	0.106458	0.510422	0.000029	0.509927	−27.8	0.4	−6.3	−10.3	2675	0.102364	0.509945	−5.4	−9.4	2599
Titanite	L2 B - c	90	2050	100	0.141551	0.510460	0.000038	0.509901	−19.8	1.2	−5.5	−8.9	2746	0.136106	0.509778	−4.1	−7.5	2634
Titanite	L2 C - c	90	2050	100	0.142010	0.510405	0.000031	0.509933	−19.2	1.2	−5.0	−8.5	2709	0.136548	0.509802	−3.6	−7.0	2597
Titanite	L2 D - r	90	1870	100	0.102045	0.510386	0.000034	0.509908	−28.8	0.4	−6.3	−10.3	2671	0.098120	0.509946	−5.3	−9.3	2598

(continued on next page)

Table 4 (*continued*)

Mineral	Grain (c/r)	Spot size (μm)	Age (Ma)	N	$^{147}Sm/^{144}Nd$ meas	$^{143}Nd/^{144}Nd$ meas	err 2se	$^{143}Nd/^{144}Nd$(i)	εNd(T0)	err 2se	Uncorrected Sm/Nd / εNd(T CHUR)	εNd(TDM)	T(DM) 2 stage	Corrected Sm/Nd / $^{147}Sm/^{144}Nd$ corr	$^{143}Nd/^{144}Nd$(i)	εNd (T CHUR)	εNd(TDM)	T(DM) 2 stage
Titanite	L2 E - c	130	2050	100	0.120588	0.510305	0.000028	0.509902	−23.0	1.8	−3.2	−6.6	2565	0.115950	0.509885	−1.9	−5.4	2470
Titanite	L2 F - c	130	2050	100	0.118604	0.510299	0.000029	0.509884	−24.6	0.6	−4.3	−7.7	2653	0.114043	0.509827	−3.1	−6.5	2559
Titanite	L2 G - r	90	1870	100	0.099819	0.510590	0.000043	0.509922	−29.4	0.3	−6.4	−10.4	2677	0.095979	0.509941	−5.4	−9.4	2605
Titanite	L2 H - c	130	2050	100	0.113216	0.510316	0.000033	0.509901	−25.7	0.7	−3.9	−7.4	2626	0.108862	0.509842	−2.8	−6.2	2536
Titanite	L2 I - c	130	2050	100	0.113927	0.511194	0.000034	0.510228	−24.6	0.9	−3.0	−6.5	2554	0.109545	0.509889	−1.9	−5.3	2464
Titanite	L2 J - r	90	1870	100	0.098240	0.511290	0.000032	0.510216	−29.9	0.3	−6.5	−10.5	2687	0.094461	0.509933	−5.6	−9.6	2617
Titanite	L2 K - r	90	1870	100	0.103130	0.511234	0.000039	0.510268	−28.5	0.3	−6.2	−10.2	2664	0.099164	0.509951	−5.2	−9.2	2590
Titanite	L2 L - c	130	2050	90	0.127645	0.511314	0.000046	0.510249	−22.4	0.5	−4.5	−7.9	2667	0.122735	0.509823	−3.2	−6.6	2566
Titanite	L2 M - c	130	2050	100	0.113208	0.511424	0.000046	0.510228	−25.6	1.6	−3.9	−7.3	2619	0.108854	0.509847	−2.7	−6.2	2529
Titanite	L2 N - c	130	2050	100	0.153698	0.511241	0.000033	0.510232	−16.4	0.9	−5.3	−8.8	2734	0.147786	0.509792	−3.8	−7.2	2612
Titanite	L2 O - c	130	2050	100	0.124966	0.511273	0.000031	0.510219	−23.5	0.9	−4.8	−8.3	2694	0.120160	0.509803	−3.6	−7.0	2595
Titanite	L2 P - c	130	2050	40	0.203127	0.511400	0.000039	0.510246	−4.1	1.1	−6.0	−9.5	2786	0.195314	0.509784	−3.9	−7.4	2625
Titanite	L2 Q - c	130	2050	100	0.123302	0.511423	0.000047	0.510224	−24.0	0.5	−4.9	−8.3	2697	0.118560	0.509801	−3.6	−7.1	2599
Titanite	L2 R - r	90	1870	100	0.097912	0.511257	0.000036	0.510272	−30.1	0.4	−6.5	−10.6	2692	0.094146	0.509930	−5.6	−9.6	2621
Titanite	RAK A	40	1850	100	0.044230	0.511288	0.000051	0.510241	−42.2	0.6	−6.2	−10.3	2649	0.042529	0.509949	−5.8	−9.9	2618
Titanite	RAK B	40	1850	100	0.040658	0.514096	0.000073	0.510254	−43.1	0.6	−6.2	−10.3	2651	0.039095	0.509946	−5.8	−9.9	2622
Titanite	RAK C	40	1850	100	0.045930	0.514101	0.000281	0.510107	−42.3	0.7	−6.7	−10.8	2690	0.044163	0.509923	−6.3	−10.4	2657
Titanite	RAK D	40	1850	100	0.038785	0.513993	0.000060	0.510240	−43.4	0.6	−6.1	−10.2	2642	0.037293	0.509951	−5.7	−9.8	2614
Titanite	RAK E	40	1850	100	0.039341	0.513924	0.000082	0.510217	−43.8	0.7	−6.6	−10.7	2680	0.037827	0.509926	−6.2	−10.3	2652
Titanite	RAK F	40	1850	100	0.033147	0.510305	0.000028	0.509902	−45.3	0.5	−6.7	−10.8	2689	0.031873	0.509917	−6.4	−10.5	2665
Titanite	RAK G	40	1850	100	0.034062	0.510299	0.000029	0.509884	−45.5	0.6	−7.1	−11.1	2715	0.032752	0.509900	−6.7	−10.8	2691
Titanite	RAK H	40	1850	100	0.054885	0.510590	0.000043	0.509922	−39.8	0.8	−6.3	−10.4	2659	0.052774	0.509947	−5.8	−9.9	2620
Titanite	RAK I	40	1850	100	0.034097	0.510316	0.000033	0.509901	−45.1	0.6	−6.7	−10.8	2691	0.032785	0.509917	−6.4	−10.5	2666
Allanite	NAU A	40	1780	100	0.082556	0.511194	0.000034	0.510228	−28.0	0.7	−2.1	−6.4	2278	0.079380	0.510265	−1.4	−5.7	2222
Allanite	NAU B	40	1780	100	0.091732	0.511290	0.000032	0.510216	−26.1	0.6	−2.3	−6.6	2296	0.088203	0.510257	−1.5	−5.8	2233
Allanite	NAU C	40	1780	100	0.082470	0.511234	0.000039	0.510268	−27.2	0.8	−1.3	−5.6	2217	0.079298	0.510305	−0.6	−4.9	2160
Allanite	NAU D	40	1780	65	0.090918	0.511314	0.000046	0.510249	−25.7	0.9	−1.7	−6.0	2246	0.087421	0.510290	−0.9	−5.2	2183
Allanite	NAU E	40	1780	100	0.102158	0.511424	0.000046	0.510228	−23.5	0.9	−2.1	−6.4	2278	0.098229	0.510274	−1.2	−5.5	2208
Allanite	NAU F	40	1780	100	0.086190	0.511241	0.000033	0.510232	−27.1	0.6	−2.0	−6.3	2271	0.082875	0.510271	−1.3	−5.5	2212
Allanite	NAU G	40	1780	100	0.090027	0.511273	0.000031	0.510219	−26.5	0.6	−2.3	−6.6	2291	0.086565	0.510260	−1.5	−5.8	2230
Allanite	NAU H	40	1780	100	0.098584	0.511400	0.000039	0.510246	−24.0	0.8	−1.8	−6.0	2251	0.094792	0.510290	−0.9	−5.2	2183
Allanite	NAU I	40	1780	100	0.102433	0.511423	0.000047	0.510224	−23.5	0.9	−2.2	−6.5	2284	0.098493	0.510270	−1.3	−5.6	2214
Allanite	NAU J	40	1780	100	0.084085	0.511257	0.000036	0.510272	−26.8	0.7	−1.2	−5.5	2210	0.080851	0.510310	−0.5	−4.8	2153
Allanite	NAU K	40	1780	100	0.089436	0.511288	0.000051	0.510241	−26.2	1.0	−1.8	−6.1	2257	0.085996	0.510282	−1.0	−5.3	2196
Titanite	NAU L	90	1780	100	0.328114	0.514096	0.000073	0.510254	28.6	1.4	−1.6	−5.9	2238	0.349057	0.510009	−6.4	−11	2013
Titanite	NAU M	90	1780	100	0.341159	0.514101	0.000281	0.510107	28.7	5.5	−4.5	−8.8	2462	0.362935	0.509852	−9.5	−14	2228
Titanite	NAU N	130	1780	100	0.320530	0.513993	0.000060	0.510240	26.6	1.2	−1.9	−6.1	2259	0.340990	0.510001	−6.6	−11	2039
Titanite	NAU O	90	1780	60	0.316595	0.513924	0.000082	0.510217	25.2	1.6	−2.3	−6.6	2295	0.336803	0.509980	−7.0	−11	2077

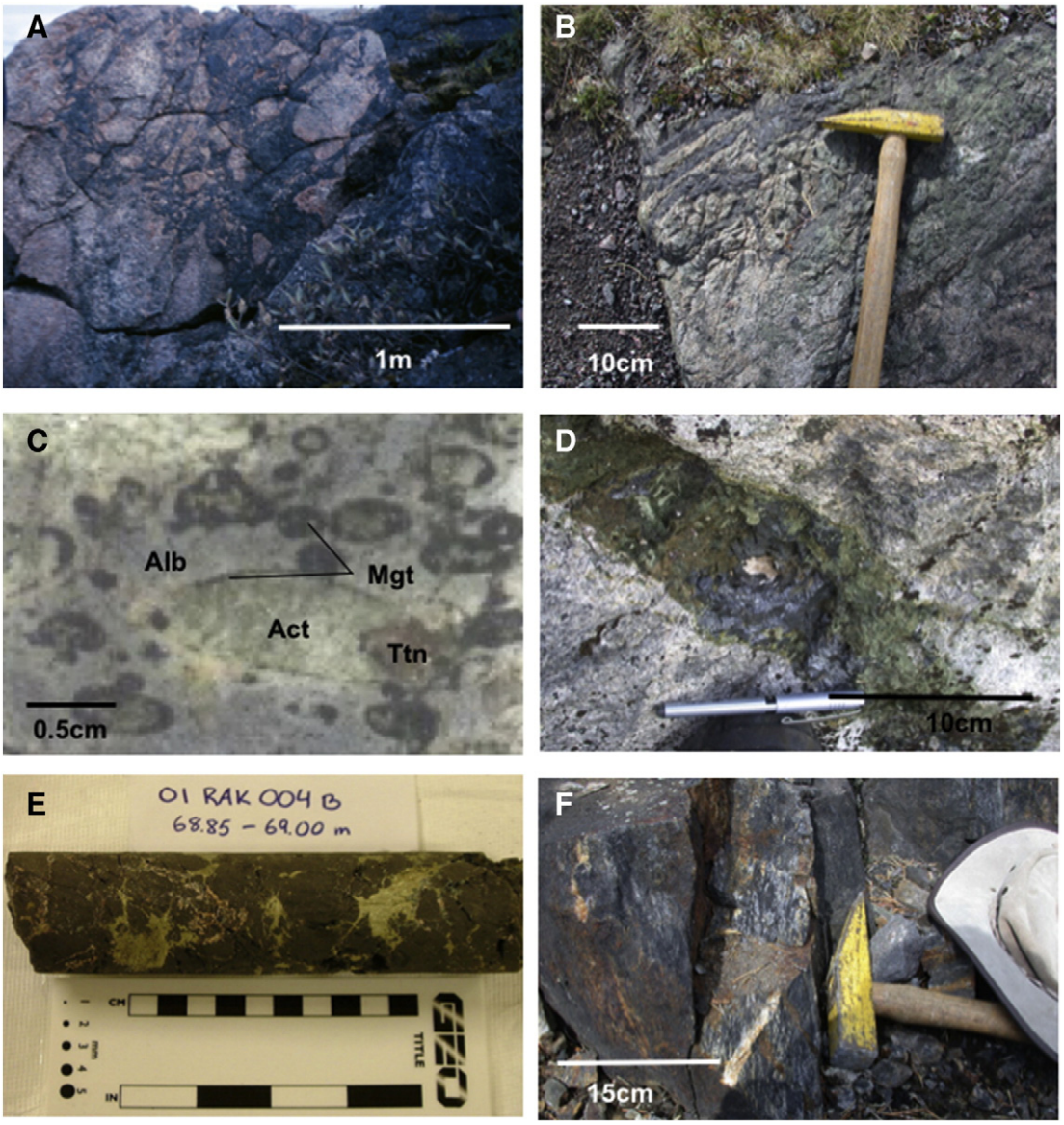

Fig. 4. Examples of mineralisation and the occurrence of titanite and allanite in samples from Norrbotten. (A) Hanging wall metavolcanic breccias cemented by magnetite, Kirunavaara. (B) Contact zone of the Luossavaara ore body. Veins of magnetite cut amygdaloidal trachy-andesite. Sample 03LUOSS01 was taken from this outcrop. (C) Cut slab photograph of 03LUOSS01 showing amygdales infilled with actinolite, magnetite and titanite. (D) Magnetite-actinolite vein cutting K—Na altered metavolcanic rock, Gruvberget. Up to 3 cm long titanite occurs within the alteration zone (see Figs. 7D, 9A). (E) Chalcopyrite cemented magnetite breccia, Rakkurijärvi. (F) Magnetite-scapolite schist from the Nautanen Deformation Zone (NDZ).

day Nd isotope ratios are distinct between the core and rim of complexly zoned grains from the hanging wall of the IOA deposit at Luossavaara and in titanite from the IOCG deposit at Gruvberget, consistent with LA-ICPMS U—Pb systematics and trace element data, and supporting interpretations of a pre-Svecofennian age for the Porphyry Group volcanic rocks (Storey et al., 2007; Fig. 9A, B). Also plotted on Fig. 10A are whole rock analyses of the associated volcanics, granitoids and Archaean basement. The mineral analyses overlap the whole rock values. This indicates that the source of metals in the alteration assemblages, and by inference in the deposits themselves, was closely linked to the source of the magmas, and that the metals were potentially derived from those granitoids. It is also clear that there is a range in εNd for a given suite of whole rocks and also from individual minerals within separate deposits. This implies that there was not one source and that they were most likely generated from hydrothermal fluids with Nd derived from crust of two (or more) discrete sources. Based on the available Sm—Nd isotope data (compiled by Bergman et al. (2001)) and local geology, the candidates for Nd sources within the magmatic rocks (granitoids) and the ore deposits are the Archaean basement and the mafic to intermediate rocks of the Greenstone and Porphyry Groups, or earlier mafic magmatism.

5. Discussion

5.1. Genesis of the deposits

As discussed above a number of models of the formation of IOA deposits invoke immiscibility between silicate and iron oxide melts with the deposits at Kiurnavaara and Luossavaara being cited as key examples of this (e.g. Nyström, 1985; Nyström and Henríquez, 1994). However, many authors argue against this (Bookstrom, 1995; Parak, 1975), and textural evidence has been cited from the early stages of magnetite mineralisation at Rakkurijärvi to show that hydrothermal magnetite mineralisation can directly replace igneous silicate rocks (Smith et al., 2007; Fig. 5C). Barton (2014) concluded that the geologic evidence is incompatible with the involvement of oxide melts in IOA and IOCG deposit

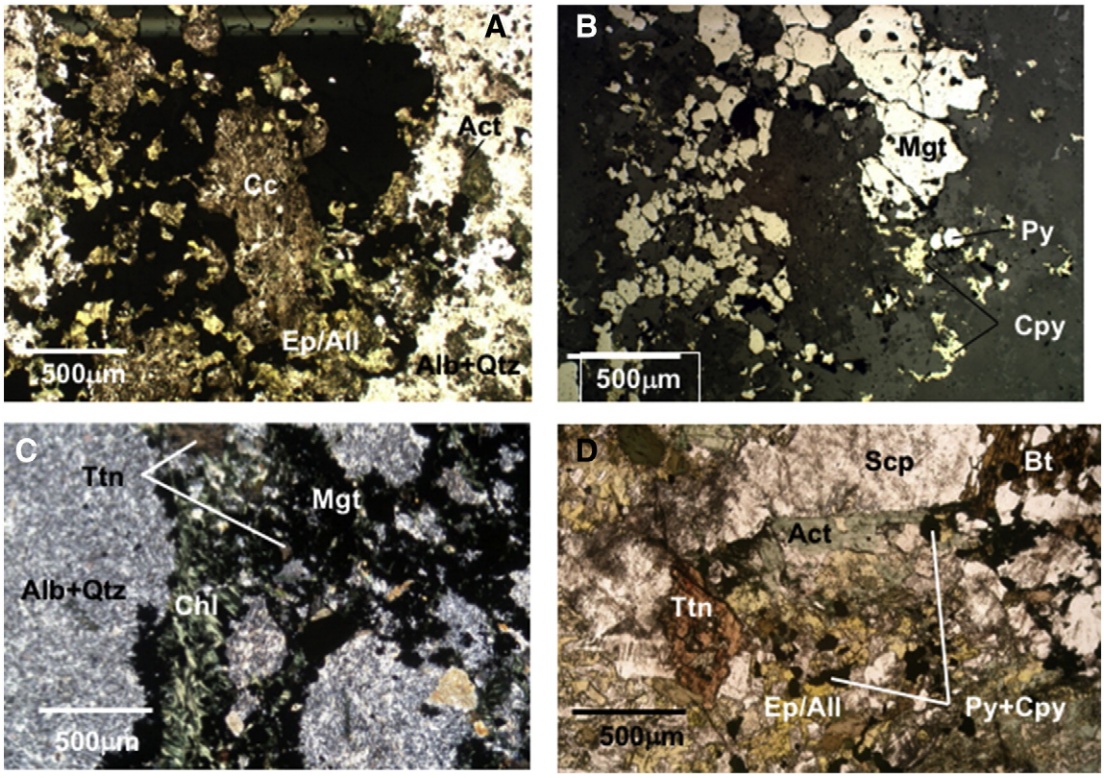

Fig. 5. Association of titanite and allanite with the ore mineral assemblage. (A) Transmitted, plane polarized light (PPL) image of amygdale developed in trachy-andesite lava, Rakkurijärvi. The amygdale infill is magnetite, epidote/allanite and calcite. (B) Reflected PPL image of (A) showing magnetite, and later association of pyrite and chalcopyrite with epidote. (C) Transmitted PPL image of magnetite-chlorite cemented breccia from Rakkurijärvi, showing titanite associated with magnetite in matrix. (D) Transmitted PPL image of scapolite-actinolite schist from Nautanen (Sample NAU84012 159.8–159.89 m), showing titanite, epidote and allanite associated with interstitial pyrite and chalcopyrite. Act – Actinolite; Alb – Albite; Qtz – Quartz; Ep – Epidote; All – Allanite; Cc – calcite; Mgt – Magnetite; Py – Pyrite; Cpy – Chalcopyrite; Chl – chlorite; Ttn – titanite; Scp – Scapolite.

genesis and points to solely hydrothermal origins. In Norrbotten, Gleeson and Smith (2010) and Smith et al. (2012) concluded that mineralising brines capable of transporting significant Fe were formed from a mixture of magmatic and external brine sources (basinal brines or evaporate dissolution), and were modified by an extensive water-rock interaction history resulting in the regional Na alteration observed in the area (Frietsch and Perdahl, 1995). These studies are consistent with IOA deposit formation via metal leaching by regional hydrothermal circulation, driven by the intrusion of the Haparanda and Perthite-Monzonite Suite granitoids, involving highly saline fluids derived from both magmatic and evaporate-related brine sources, followed by magnetite deposition either in breccias or via host rock replacement in structurally favourable sites. Such models are consistent with work elsewhere, notably the Cloncurry district Australia (Oliver et al., 2004). Copper mineralisation in the district is distinct from the IOA deposits, with chalcopyrite mineralisation typically *syn*- to post-magnetite deposition. Iron oxide-copper-gold type mineralisation is spatially associated with magnetite-apatite mineralisation at sites including Rakkurijärvi and Gruvberget. However, fluid inclusion studies (Broman and Martinsson, 2000; Smith et al., 2012) indicate distinctions in fluid chemistry between IOA and IOCG deposits. In sulphide mineralised deposits, sulphur isotope studies are consistent with hydrothermal fluid interaction with a wide range of country rocks (Frietsch et al., 1995) and halogen chemistry from both deposit types is again consistent with mixing of brines of different sources. The Cu deposits associated with the Nautanen Deformation Zone are significantly later than the other deposits (~1.7–1.8Ga), and are the most Cu-rich of the area. The features of the deposit along the NDZ, including the Aitik deposit, are consistent with modification of initial IOCG-type mineralisation by subsequent aqueous-carbonic fluids during deformation (Broman and Martinsson, 2000; Wanhainen et al., 2003; Smith et al., 2012). None of these models have as yet addressed the source of metals.

5.2. Metal sources during mineralisation

The IOA deposits of the Kiruna district formed synchronously with local subduction granitoids (Smith et al., 2009), and Nd isotope ratios are consistent with derivation of the REE from those granitoids. A correlation between the Ni, Cu and REE concentration in titanite from Norrbotten was noted by Smith et al. (2009). Smith et al. (2012) argued that the primary, hydrothermal, Cu transport in the IOCG deposits of the district was by chloride complexes, although bisulphide may have been important in remobilisation of the ores at Nautanen and Aitik, and it has now been demonstrated that REE transport is also most likely as chloride complexes (Migdisov et al., 2009; Williams-Jones et al., 2013). Depleted mantle model ages indicate that the granitoids themselves derived Nd from melting of basic rocks formed around 2.5 Ga with minor contributions from older (c.2.8 Ga) Archaean basement (Figs. 10, 11). It is also possible that the Nd isotope signature of the granitoids may be derived from mixing of Archaean materials with juvenile magmas derived from enriched sources, although little basic magmatism of post-Greenstone group age is exposed in the area. Neodymium in the IOA deposits was derived from similar sources, either directly from magmatic-hydrothermal processes, or more likely from regional fluid circulation through the Svecokarelian rocks and Svecofennian granitoids with contributions from multiple fluid sources (Frietsch et al., 1997; Gleeson and Smith, 2010). The initial phase of IOCG mineralisation in the area occurred after this, during continental collision and amalgamation with a potentially slightly wider range of Nd sources and leaching from a range of host rocks (Fig. 10B, C). It is notable that the most Cu and Au-rich deposit in this study (the modified IOCG deposits at Nautanen) show the highest εNd values, and hence the greatest metal input from the most juvenile crust. None the less, these still exhibit negative $\varepsilon Nd_{(t,CHUR)}$ suggesting significant crustal residence times for the metal source (Fig. 10A), probably derived by

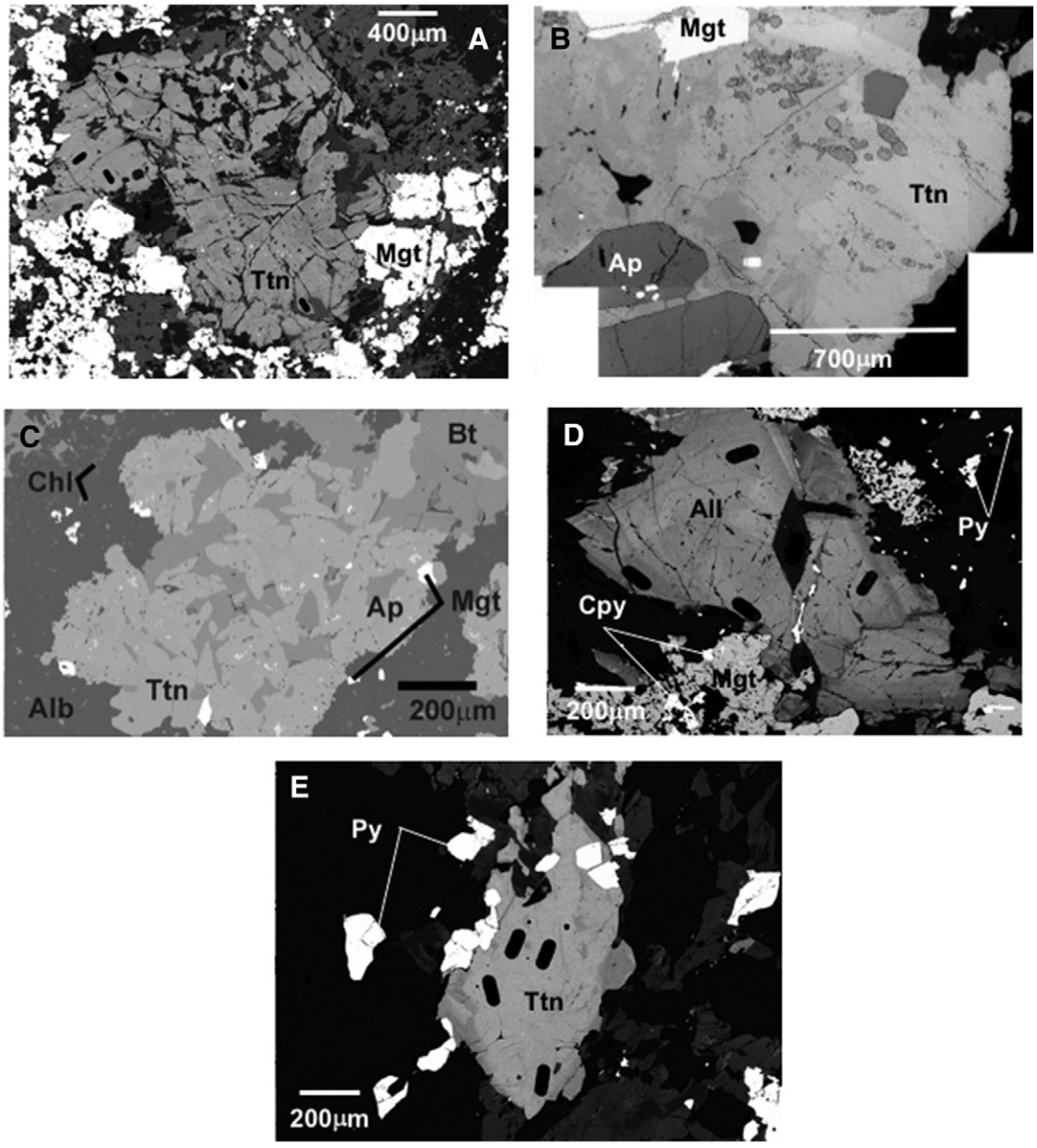

Fig. 6. Back scattered electron images of internal textures of titanite and allanite. (A) Backscattered electron (BSE) image of titanite associated with magnetite from Luossavaara (03LUOSS01). (B) Titanite overgrowing magnetite and apatite, Valkommen (03VALK01). (C) Amygdale infilled with titanite, apatite and biotite, Rakkurijärvi (01RAK006 183.0 m). (D) BSE image of allanite from vug in altered trachy-andesite, Rakkurijärvi (01RAK006 183.0 m). (E) Titanite intergrown with pyrite, Nautanen NAU84012 159.8–159.89 m. Mineral abbreviations as in Fig. 5, plus Ap – apatite. Lozenge shapes in each case are ablation pits from U–Pb analyses carried out prior to Sm–Nd isotope analyses.

leaching of the Greenstone group mafic volcanics. Although Nd isotope systematics cannot directly trace the source of ore metals (Fe, Cu), the variation in REE source inferred here suggests that a similar variation in the source of ore metals may account for differences in metal content between deposits. Overall the data are consistent with previous studies of IOCG and IOA deposits, which indicated that metals were derived from local host rocks of a range of ages, rather than a single, specialised magmatic source (Gleason et al., 2000).

5.3. Relation of metal source and mineralising processes to the continental cycle

Relation of the timing and metal source within the Kiruna district requires a brief review of the evolution of the Fennoscandian shield through this time period. The amalgamation of cratons at the end of the Neoarchaean (c.2.7 to 2.5 Ga ago) resulted in the accretion of mafic volcanics as greenstones on to the margin of the gneissic Archaean craton core (Weihed et al., 2005). This was followed by the initiation of rifting of the supercontinent/supercraton, manifested as global mafic magmatism in the time period 2.5–2.4 Ga (Kullerud et al., 2006; Davies and Heaman, 2014) and earliest possible ages of the Greenstone Group of northern Sweden (Weihed et al., 2005). Breakup of the supercontinent so that plates began to drift, with a resultant return to magmatism at arcs, began at around 2.2 Ga ago (Kullerud et al., 2006). The formation of evolved volcanic rocks in northern Sweden, the Porphyry Group, proceeded around 2.1 Ga ago (Storey et al., 2007). Subsequent amalgamation of plates into a supercontinental configuration (i.e. Nuna/Columbia) was achieved between 1.9 and 1.3 Ga ago (Evans and Mitchell, 2011).

The imprint in northern Sweden of this amalgamation is the Svecokarelian orogeny and magmatism, in an arc to post-collisional setting, which occurred between 1.9 and 1.8 Ga ago. The period involved

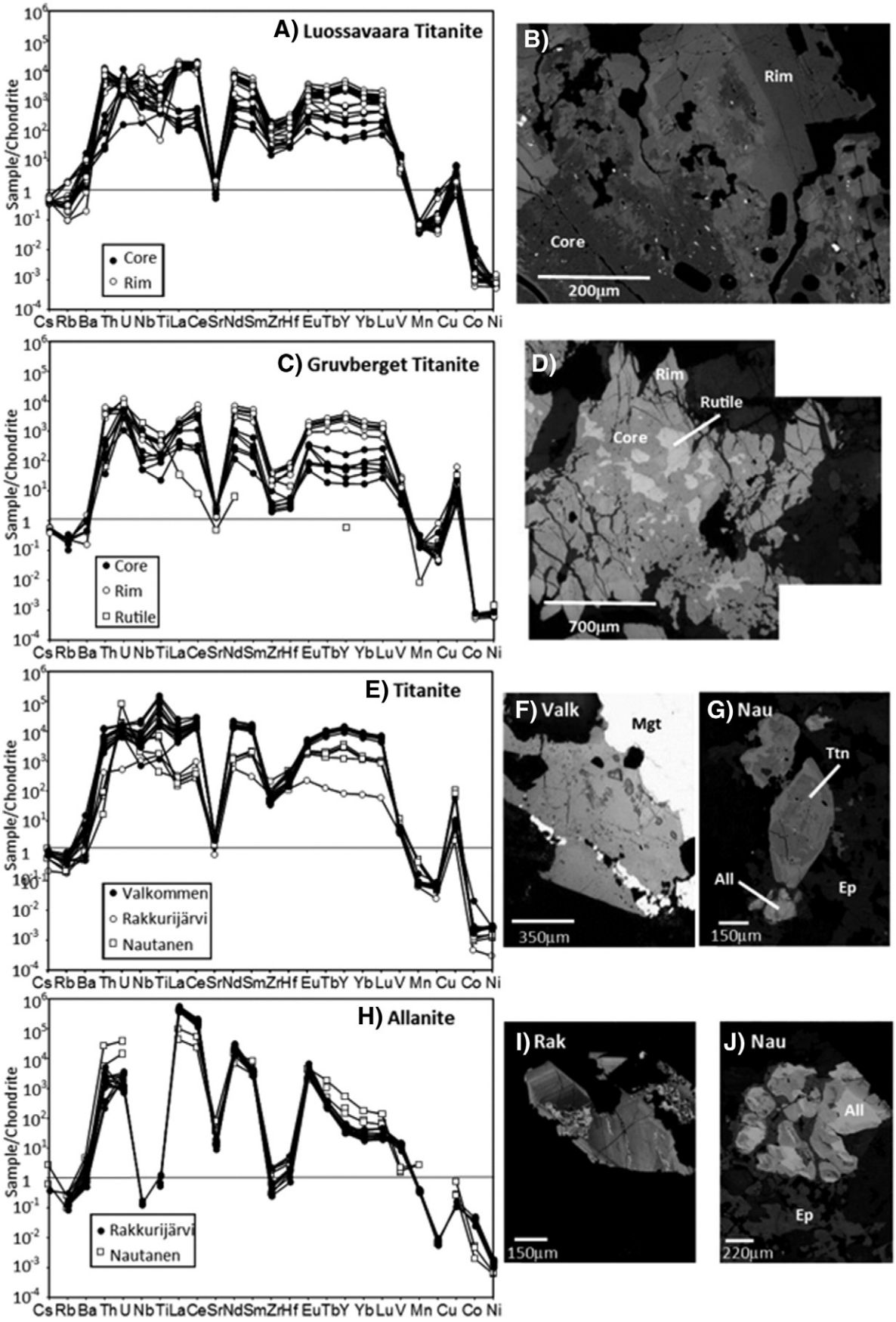

Fig. 7. Results of previous LA-ICPMS analyses of trace element compositions of titanite and allanite analysed, with examples of analysed grains. (A) and (B) Compositionally zoned titanite from Luossavaara. (C) and (D) Compositionally zoned titanite nucleated on rutile from Gruvberget. (E) (F) and (G) Individual titanite grains from Valkommen, Rakkurijärvi and Nautanen. (H), (I) and (J) Individual allanite grains from Rakkurijärvi and Nautanen. All data from Smith et al. (2009).

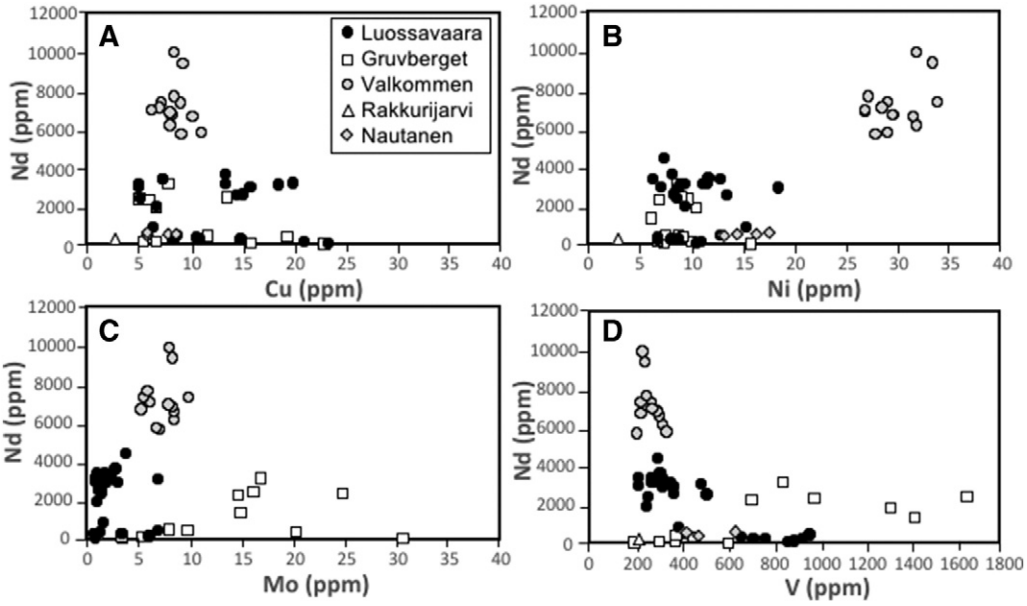

Fig. 8. Comparison of Nd concentration with transition metal concentrations in titanite.

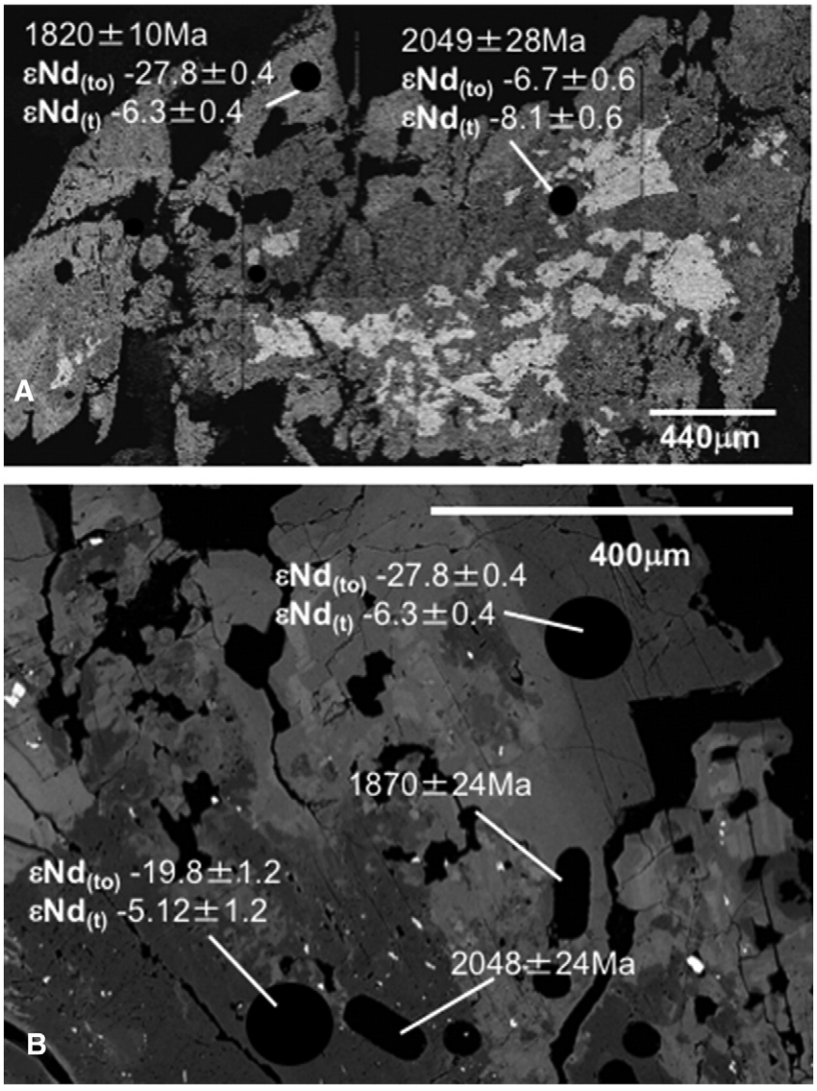

Fig. 9. Examples of isotopic heterogeneity and textures in titanites and allanites from IOA and IOCG deposits. (A) Gruverberget (B) Titanite from Luossavaara. Ages are from Storey et al. (2007), Nd isotope data from this study. Ages in A are from texturally corresponding zones in other crystals.

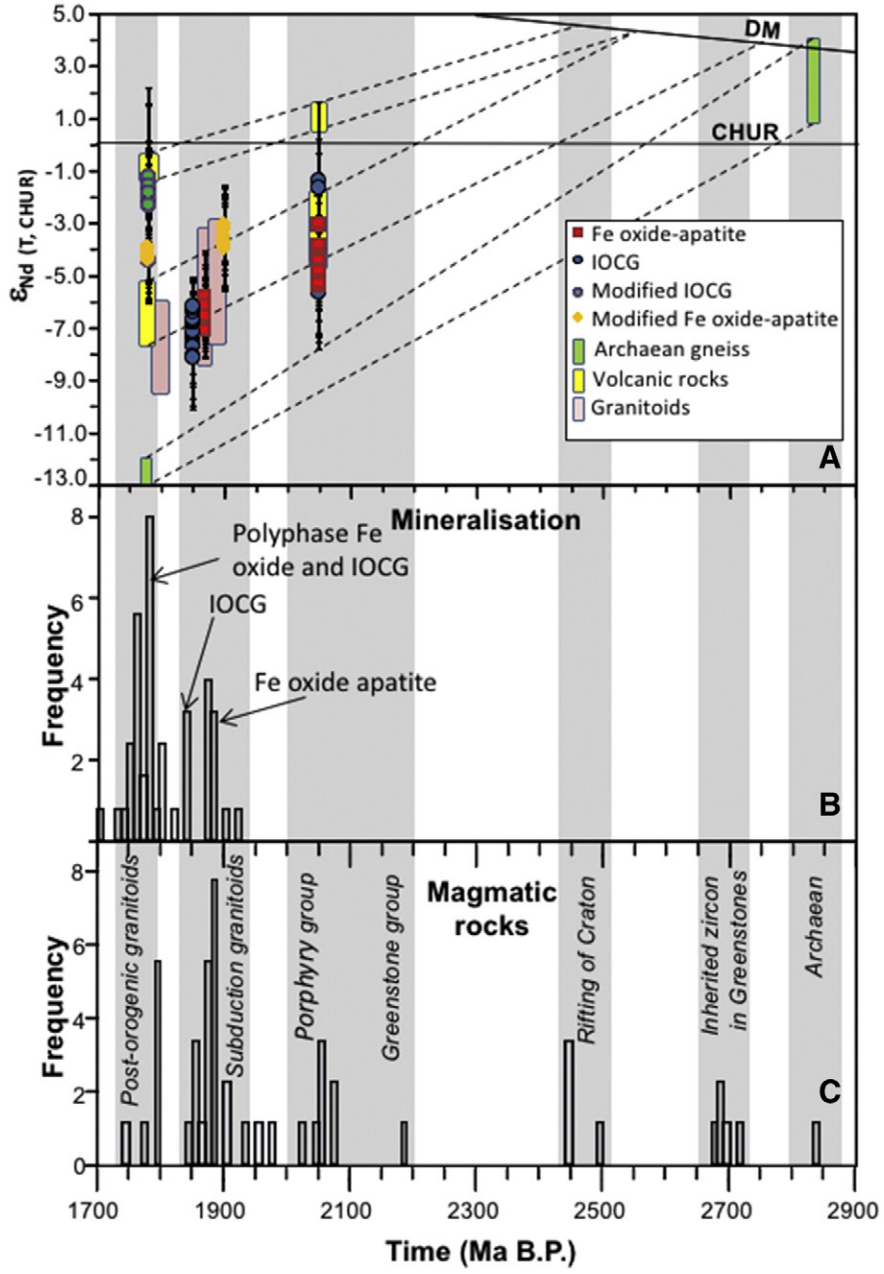

Fig. 10. (A) Evolution trends of $e_{Nd\ (T,\ CHUR)}$ for crustal reservoirs in the Fennoscandian shield, compared with the composition of granitoids (Bergman et al., 2001), and in situ determinations of titanite $e_{Nd\ (T,\ CHUR)}$ from this study. (B) Histogram of U—Pb ages for magmatic zircon and titanite from the Norrbotten area of the Fennoscandian Shield (References in Supplementary Material). (C) Histogram of U—Pb ages of mineralisation related titanite, monazite and zircon (References in Supplementary Material).

subduction, followed by accretion of a series of microcontinental blocks and island arcs (Weihed et al., 2005). At the same time, hydrothermal activity related to the magmatism mobilised and concentrated iron, copper and gold into economic deposits. As we have shown for the REE's, the ultimate source of the metals in subduction granitoids and related deposits is likely to be pre-existing mafic igneous rocks related to accreted Archaean greenstones, the early rifting phase, and the Greenstone Group, (Figs. 10, 11). Older Archaean model ages suggest that some remelting of evolved gneissic material from the core of the craton occurred, resulting in a range of model ages. The major magmatic arc and collisional belt, the Svecokarelian orogeny, provided energy and fluid sources for remobilisation of metals from this mafic juvenile crust and, as the plates were organised into a supercontinental configuration, the preservation potential of both magmatism and mineralisation was much higher than at other times (Hawkesworth et al., 2009). Thus, the major peak of global IOCG deposits during this period (Groves et al., 2010) can be explained in the context of a supercontinent cycle. A number of authors have argued that primary mafic melts are not especially enriched in Cu, but that formation of cumulates enriched in Cu, which are deeply buried during arc building, are the likely source for subsequent hydrous, oxidized melts (Richards, 2009; Lee et al., 2012). This is consistent with a two-stage model for the source and final liberation of metals and implies a time lag between source emplacement and liberation of c.5–600 Ma during a period of subsequent crustal thickening and arc magmatism (Figs. 10, 11). A similar incubation period has been suggested for the formation of evolved crust recorded by the Hf isotope composition of zircons (Lancaster et al., 2011). If the incubation time for bulk continental crust (time from

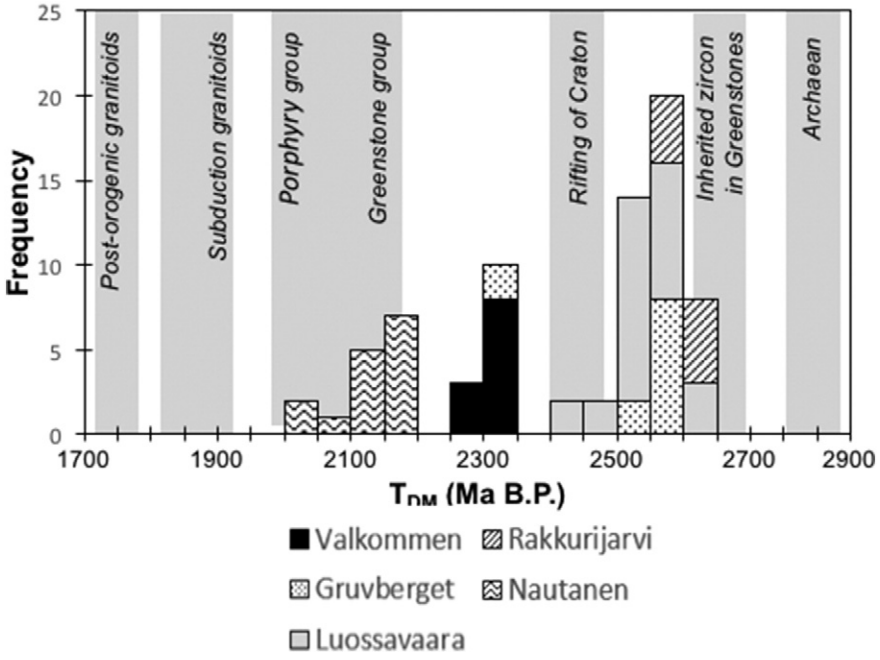

Fig. 11. Distribution of two stage depleted mantle model ages for titanite and allanite, calculated assuming a crustal Sm/Nd ratio of 0.12. The timings of recognised tectonic events in the evolution of the Fennoscandian shield are shown for reference.

mantle separation to crystallisation in an evolved melt) is the same as that for enriched Cu sources (from mantle separation to mineralisation) then it is likely that a similar tectonic process is responsible. This supports the proposed link between supercontinent formation, continental crust and economic metal preservation.

The conclusion that metals in ICOG and IOA systems were derived from mafic crust generated in early phases of tectonic activity is not inconsistent with previous attempts to link metal and ligand source with tectonic setting (Groves et al., 2010) and secular changes in subduction systems (Richards and Mumin, 2013). Both would have metal sources in previously enriched sub-continental lithospheric mantle. However, the conclusion that the temporal peak of these deposits around 1.8 Ga in Fennoscandia is related to increased preservation potential in arc-accretion and post-collisional settings, is at odds with Richards and Mumin's (2013) conclusion that igneous-related IOCG systems are restricted to the Proterozoic because of a major change in ocean sulphate chemistry at the end of the Precambrian. It is not clear that any of these deposits exclusively involved magmatic fluids (e.g. Kendrick et al., 2007; Smith et al., 2012; Barton, 2014). Equally, the major Phanerozoic systems occur in the Andes (Groves et al., 2010), where they are in ocean-facing arc settings which will give them a similar erosion potential, and hence half-life in the geological record, as porphyry Cu-systems. The critical factors seem to be a potential source of high Cl concentrations (be they magmatic or sedimentary) and, as shown here, the presence of lithosphere fertilised by mantle melts either during an earlier phase of subduction, or during previous rift or plume related magmatism.

6. Conclusions

The age distribution of igneous rocks within the Fennoscandian shield shows that early Palaeoproterozoic events were dominated by basic and ultramafic magmas generated in oceanic and extensional settings. Evolved igneous rocks do not occur until the onset of accretion of the supercontinent Nuna/Columbia, nor do IOCG type mineral deposits. However, Nd isotope data indicate that the subduction and orogenic grantioids are not the sole source of Nd, and by inference other metals, for the IOCG mineralisation, but pre-existing, more basic sources are implicated. The results imply that fertile mafic crust was incubated under and on the margins of the Archaean craton in the early Palaeoproterozoic. However, mineralisation did not occur, or at least was not preserved, until an arc was initiated at the margin during a period of continental amalgamation, i.e. ocean closure, and hence provided a heat and fluid source for mobilisation and concentration of the metals.

The tectonic setting of IOCG mineralisation is such that Mesozoic and Cainozoic examples occur dominantly in ocean-facing continental arc settings (the Andes; Groves et al., 2010), whilst those in the older geological record are dominantly in collisional and post-orogenic settings. This strongly indicates that the history of mineralisation for this style of deposit is affected by a preservation bias. However, Nd isotope data also show unequivocally that the formation of metal-enriched crust via basic magmatism in pre-orogenic settings was critical in the formation of economic mineral resources. Undoubtedly mineralising processes occurred throughout the period of supercontinent/craton dispersion (Weihed et al., 2005), but renewed continental collision provided both heat, and magmatic and hydrothermal fluid sources, for remobilisation of metals from older, juvenile crust in tectonic settings with high potential for subsequent long term preservation. The incubation time for economic mineralisation is the same as for bulk continental crust, thus arguing for related processes and according well with the supercontinent cycle.

Acknowledgments

We thank Chris Hawkesworth and Bruno Dhuime for comments on an earlier draft. CS acknowledges NERC Fellowship NE/D0088911/1 and MS acknowledges EU RDF Georange Program Grant 89121.

Appendix A. Supplementary data

Supplementary data to this article can be found online at http://dx.doi.org/10.1016/j.oregeorev.2016.08.035.

References

Barton, M.D., 2014. Iron Oxide(–Cu–Au–REE–P–Ag–U–Co) Systems. Treatise on Geochemistry. 2nd Edition. pp. 515–541.

Barton, M.D., Johnson, D.A., 1996. Evaporitic-source model for igneous-related Fe oxide-(REE-Cu-Au-U) mineralization. Geology 24, 259–262.

Barton, M.D., Johnson, D.A., 2000. Alternative brine sources for Fe-oxide(-Cu-Au) systems: implications for hydrothermal alteration and metals. In: Porter, T.M. (Ed.), Hydrothermal Iron Oxide Copper^Gold and Related Deposits: A Global Perspective. Adelaide, Australian Mineral Foundation, pp. 43–60.

Bergman, S., Küber, L., Martinsson, O., 2001. Description of the regional geological and geophysical maps of Northern Norrbotten County (east of the Caledonian orogen). SGU Ba 56 (110 p).

Blake, K., 1990. The petrology, geochemistry and association to ore formation of the host rocks of the Kiirunavaara magnetite-apatite deposit, northern Sweden. PhD thesis, University of Wales, Cardiff.

Bookstrom, A., 1995. Magmatic features of iron ores of the Kiruna type in Chile and Sweden: ore textures and magnetite geochemistry: a discussion. Econ. Geol. 90, 469–475.

Broman, C., Martinsson, O., 2000. Fluid inclusions in epigenetic Fe–Cu–Au ores in Northern Norrbotten. In: ·Weihed, P., Martinsson, O. (Eds.), 2nd Annual GEODE Fennoscandian Shield Workshop on Palaeo-Proterozoic and Archaean greenstone belts and VMS districts in the Fennoscandian Shield: Gallivare-Kiruna. Sweden 6. Lulea° Univeristy of Technology Research Report, p. 7.

Campbell, I., Allen, C., 2008. Formation of supercontinents linked to increases in atmospheric oxygen. Nat. Geosci. 1, 554–558.

Clift, P.D., Hartley, A.J., 2007. Slow rates of subduction erosion and coastal underplating along the Andean margin of Chile and Peru. Geology 35, 503–506.

Condie, K.C., 1998. Episodic continental growth and supercontinents: a mantle avalanche connection? Earth Planet. Sci. Lett. 163, 97–108.

Condie, K.C., Aster, R.C., 2010. Episodic ziron age spectra of orogenic granitoids: the supercontinental connection and continental growth. Precambrian Res. 180, 227–236.

Davies, J.H.F.L., Heaman, L.M., 2014. New U-Pb baddeleyite and zircon ages for the Scourie dyke swarm: a long-lived igneous province with implications for the Palaeoproterozoic evolution of NW Scotland. Chem. Geol. 249, 180–198.

Evans, D.A.D., Mitchell, R.N., 2011. Assembly and breakup of the core of Paleoproterozoic-Mesoproterozoic supercontinent Nuna. Geology 39, 443–446.

Foster, G.L., Vance, D., 2006. In situ Nd isotopic analysis of geological materials by laser ablation MC-ICP-MS. J. Anal. At. Spectrom. 21, 288–296.

Frietsch, R., Perdahl, J.-A., 1995. Rare earth elements in apatite and magnetite in Kiruna-type iron ores and some other iron ore types. Ore Geol. Rev. 9, 489–510.

Frietsch, R., Billstrœm, K., Perdahl, J.-A., 1995. Sulphur isotopes in Lower Proterozoic iron and sulphide ores in northern Sweden. Mineral. Deposita 30, 275–284.

Frietsch, R., Tuisku, P., Martinsson, O., Perdahl, J.-A., 1997. Early Proterozoic Cu-(Au) and Fe ore deposits associated with regional Na-Cl metasomatism in northern Fennoscandia. Ore Geol. Rev. 12, 1–34.

Gleason, J.D., Marikos, M.A., Barton, M.D., Johnson, D.A., 2000. Neodymium isotopic study of rare earth element sources and mobility in hydrothermal Fe oxide (Fe-P-REE) systems. Geochim. Cosmochim. Acta 64, 1059–1068.

Gleeson, S.A., Smith, M.P., 2010. The sources and evolution of mineralising fluids in iron oxide-copper-gold systems, Norrbotten, Sweden: constraints from Br/Cl ratios and stable Cl isotopes of fluid inclusion leachates. Geochim. Cosmochim. Acta 73, 5658–5672.

Goldfarb, R.J., Bradley, D., Leach, D.L., 2010. Secular variation in economic geology. Econ. Geol. 105, 459–465.

Groves, D.I., Bierlein, F.P., Meinert, L.D., Hitzman, M.W., 2010. Iron Oxide Copper-Gold (IOCG) deposits through Earth history: implications for origin, lithospheric setting, and distinction from other epigenetic iron oxide deposits. Econ. Geol. 105, 641–654.

Hawkesworth, C.J., Cawood, P.A., Kemp, A.I.S., Storey, C., Dhuime, B., 2009. A matter of preservation. Science 323, 49.

Hitzman, M.W., 2000. Iron oxide-Cu-Au deposits: what, where, when and why. In: Porter, T.M. (Ed.), Hydrothermal iron oxide copper-gold and related deposits: a global perspective. Aus. Min. Found., Glenside, Australia, pp. 9–26.

Hitzman, M.W., Oreskes, N., Einaudi, M.T., 1992. Geological characteristics and tectonic setting of Proterozoic iron-oxide (Cu-U-Au-REE) deposits. Precambrian Res. 58, 241–287.

Kendrick, M.A., Mark, G., Phillips, D., 2007. Mid-crustal fluid mixing in a Proterozoic Fe oxide–Cu–Au deposit, Ernest Henry, Australia: evidence from Ar, Kr, Xe, Cl, Br, and I. Earth Planet. Sci. Lett. 256, 328–343.

Kendrick, M.A., Honda, M., Gillen, D., Baker, T., Phillips, D., 2008. New constraints on regional brecciation in the Wernecke Mountains, Canada from He, Ne, Ar, Kr, Xe, Cl, Br and I in fluid inclusions. Chem. Geol. 255, 33–36.

Kesler, S.E., Wilkinson, B.H., 2008. Earth's copper resources estimated from tectonic diffusion of porphyry copper deposits. Geology 36, 255–258.

Kullerud, K., Skjerlie, K., Corfu, F., de la Rosa, J.D., 2006. The 2.40 Ga Ringvassøy mafic dykes, west Troms basement complex, Norway: the concluding act of early Palaeoproterozoic continental breakup. Precambrian Res. 150, 183–200.

Lahtinen, R., Huhma, H., Kousa, J., 2002. Contrasting source components of the Paleoproterozoic Svecofennian metasediments: detrital zircon U-Pb, Sm-Nd and geochemical data. Precambrian Res. 116, 81–109.

Lancaster, P.J., Storey, C.D., Hawkesworth, C.J., Dhuime, B., 2011. Understanding the roles of crustal growth and preservation in the detrital zircon record. Earth Planet. Sci. Lett. 305, 405–412.

Lee, C.-T.A., Luffi, P., Chin, E.J., Bouchet, R., Dasgupta, R., Morton, D.M., Le Roux, V., Yin, Q.-Z., Jin, D., 2012. Copper systematics in arc magmas and implications for crust-mantle differentiation. Science 336, 64–68.

Martinsson, O., 2004. Geology and metallogeny of the Northern Norrbottn Fe–Cu–Au province. Soc. Econ. Geol. 33, 131–158.

Mathur, R., Marschik, R., Ruiz, J., Munizaga, F., Leveille, R.A., Martin, W., 2002. Age of mineralization of the Candelaria Fe oxide Cu-Au deposit and the origin of the Chilean iron belt, based on Re-Os isotopes. Econ. Geol. 57, 59–71.

Mcfarlane, C.R.M., McCulloch, M.T., 2007. Coupling of in-situ Sm-Nd systematics and U-Pb dating of monazite and allanite with applications to crustal evolution studies. Chem. Geol. 245, 45–60.

Migdisov, A.A., Williams-Jones, A.E., Wagner, T., 2009. An experimental study of the solubility and speciation of the Rare Earth Elements (III) in fluoride- and chloride-bearing aqueous solutions at temperatures up to 300 °C. Geochim. Cosmochim. Acta 73, 7087–7109.

Nyström, J.O., 1985. Apatite iron ores of the Kiruna Field, northern Sweden: Magmatic textures and carbonatitic affinity. GFF. 107, 133–141.

Nyström, J.O., Henríquez, F., 1994. Magmatic features of iron of the Kiruna type in Chile and Sweden: ore textures and magnetite geochemistry. Econ. Geol. 89, 820–839.

Oliver, N.H.S., Cleverley, J.S., Mark, G., Pollard, P.J., Fu, B., Marshall, L.J., Rubenach, M.J., Williams, P.J., Baker, T., 2004. Modelling the role of sodic alteration in the genesis of iron oxide-copper-gold deposits, eastern Mount Isa block, Australia. Econ. Geol. 99, 1145–1176.

Parak, T., 1975. Kiruna iron ores are not 'intrusive magmatic ores of the Kiruna type'. Econ. Geol. 70, 1242–1258.

Pollard, P.J., 2006. An intrusion-related origin for Cu-Au mineralization in iron oxide-copper-gold (IOGG) provinces. Mineral. Deposita 41, 179–187.

Putnis, A., 2002. Mineral replacement reactions: from macroscopic observations to microscopic mechanisms. Mineral. Mag. 66, 689–708.

Richards, J.P., 2009. Post-subduction porphyry Cu-Au and epithermal Au deposits: products of remelting of subduction-modified lithosphere. Geology 37, 247–250.

Richards, J.P., Mumin, A.H., 2013. Magmatic-hydrothermal processes with an evolving Earth: iron oxide-copper-gold and porphyry Cu ± Mo ± Au deposits. Geology 41, 767–770.

Romer, R., Martinsson, O., Perdahl, J.-A., 1994. Geochronology of the Kiruna iron ores and hydrothermal alterations. Econ. Geol. 89, 1249–1261.

Romer, R., Martinsson, O., Perdahl, J.-A., 1996. Scapolite: a tracer for the initial lead isotopic composition in sulphide deposits with later additions of radiogenic lead. Mineral. Deposita 31, 134–139.

Skiöld, T., 1987. Aspects of the Proterozoic geochronology of northern Sweden. Precambrian Res. 35, 161–167.

Skiöld, T., 1988. Implications of new U-Pb zircon chronology to early Proterozoic crustal accretion in northern Sweden. Precambrian Res. 32, 35–44.

Smith, M.P., Coppard, J., Herrington, R., Stein, H., 2007. The geology of the Rakkurijärvi Cu-(Au) prospect, Norrbotten: a new IOCG deposit in Northern Sweden. Econ. Geol. 102, 393–414.

Smith, M.P., Storey, C.D., Jeffries, T.E., Ryan, C., 2009. In situ U-Pb and trace element analysis of accessory minerals in the Kiruna District, Norrbotten, Sweden: new constraints on the timing and origin of mineralization. J. Petrol. 50, 2063–2094.

Smith, M.P., Gleeson, S.A., Yardley, B.W.D., 2012. Hydrothermal fluid evolution and metal transport in the Kiruna District, Sweden: contrasting metal behaviour in aqueous and aqueous-carbonic brines. Geochim. Cosmochim. Acta 102, 89–112.

Storey, C.D., Smith, M., Jeffries, T., 2007. In situ LA-ICP-MS U-Pb dating of metavolcanics of Norrbotten, Sweden: records of extensive geological histories in complex titanite grains. Chem. Geol. 240, 163–181.

Wanhainen, C., Broman, C., Martinsson, O., 2003. The Aitik Cu-Au-Ag deposit in northern Sweden: a product of high salinity fluids. Mineral. Deposita 38, 715–726.

Wanhainen, C., Billström, K., Martinsson, O., Stein, H., Nordin, R., 2005. 160 Ma of magmatic/hydrothermal and metamorphic activity in the Gällivare area: Re-Os dating of molybdenite and U-Pb dating of titanite from the Aitik Cu-Au-Ag deposit, northern Sweden. Mineral. Deposita 40, 435–447.

Wasserburg, J.G., Jacobsen, S.B., DePaolo, D.J., McCulloch, M.T., 1981. Precise determination of Sm/Nd ratios, Sm and Nd isotopic abundances in standard solutions. Geochim. Comsochim. Acta. 45, 2311–2323.

Weihed, P., Arndt, N., Billström, K., Duchesne, J.C., Eilu, P., Martinsson, O., Papunen, H., Lahtinen, R., 2005. Precambrian geodynamics and ore formation: the Fennoscandian shield. Ore Geol. Rev. 27, 273–322.

Williams, P.J., Barton, M.D., Johnson, D.A., Fontbote, L., de Haller, A., Mark, G., Oliver, N.H.S., Marschik, R., 2005. Iron oxide copper-gold deposits: geology, space-time distribution, and possible modes of origin. Econ. Geol. 100, 371–405.

Williams-Jones, A.E., Migdisov, A.A., Samson, I.M., 2013. Hydrothermal mobilisation of the rare earth elements - a tale of "ceria" and "Yttria". Elements 8, 355–360.